ANNUAL REVIEWS

Annual Review of Fluid Mechanics

Fluid Dynamics of Airtanker Firefighting

Dominique Legendre

Institut de Mécanique des Fluides de Toulouse (IMFT), CNRS UMR 5502, Institut national polytechnique de Toulouse (INPT), Université Paul Sabatier (UPS), Université de Toulouse, Toulouse, France; email: dominique.legendre@imft.fr

Annu. Rev. Fluid Mech. 2024. 56:577–603

First published as a Review in Advance on October 31, 2023

The *Annual Review of Fluid Mechanics* is online at fluid.annualreviews.org

https://doi.org/10.1146/annurev-fluid-121021-041642

Keywords

airtanker firefighting, droplet, atomization, dispersion, droplet impact, droplet evaporation, rainfall, canopy interception, Newtonian and non-Newtonian fluids

Abstract

Airtanker firefighting is the most spectacular tool used to fight wildland fires. However, it employs a rudimentary large-scale spraying technology operating at a high speed and a long distance from the target. This review gives an overview of the fluid dynamics processes that govern this practice, which are characterized by rich and varied physical phenomena. The liquid column penetration in the air, its large-scale fragmentation, and an intense surface atomization give shape to the rainfall produced by the airtanker and the deposition of the final product on the ground. The cloud dynamics is controlled by droplet breakup, evaporation, and wind dispersion. The process of liquid deposition onto the forest canopy is full of open questions of great interest for rainfall retention in vegetation. Of major importance, but still requiring investigation, is the role of the complex non-Newtonian viscoelastic and shear-thinning behavior of the retardant dropped to stop the fire propagation. The review describes the need for future research devoted to the subject.

1. INTRODUCTION

1.1. Airtanker Firefighting

Airtanker: an aerial device used to drop liquid, such as a helicopter with a bucket or transformed civil or military airplanes

Drop: to release a liquid from a flying aircraft

Airtanker firefighting is the most spectacular tool used to fight wildland fires. Some airtankers, such as Traker or Canadair aircraft, drop water directly onto the fire to cool it down and wet it enough to extinguish the fire (see **Figure 1*a***). Other airtankers, such as Dash-8, BAe-146, or DC-10, are used to deposit a barrier of fire retardant ahead of the advancing fire front to guide or stop the fire's propagation (see **Figure 1*b***). Each type of airtanker deserves a global strategy used to fight a given fire in coordination with ground firemen. The so-called direct attack requires airtanker delivery systems that can drop several tons of water in a short time (typically 1–2 s). The deposit of retardant barriers requires delivery systems that can generate regular and concentrated lines of retardant.

Dropping a liquid from an aircraft is a natural process that is easy to achieve because the released liquid directly falls to the ground due to gravity. Currently, the optimization and development of airtankers are mostly based on empirical methods, and performance is assessed using the cup-and-grid method (Suter 2000), whereby the dropped liquid is collected on a grid of cups distributed on a field without vegetation. However, the drop performance of each airtanker is specific to the individual aircraft and largely unpredictable: As much as 45% of the released volume can evaporate or be dispersed and not contribute to the drop pattern. The liquid deposit is usually not uniform, and along the drop pattern centerline where the liquid concentration is expected to be maximum and uniform, variation of concentration larger than 50% can be observed, thus creating preferential paths for the fire to continue to spread (Legendre et al. 2013).

Since the first operational drops in the mid-1950s, several aircraft, ranging from agricultural spray planes to military transports, have been transformed into airtankers. In 1969, the US Forest Service initiated research studies to quantify and improve airtanker performance. These studies entailed dropping different liquids (retardant or water) over a sampling grid to analyze the ground pattern under a variety of conditions in order to provide airtanker performance guidelines (George & Johnson 1990).

Curiously, the scientific community has not yet seriously considered the fragmentation process of a liquid injected in an air cross flow at sizes and conditions of interest for aerial firefighting

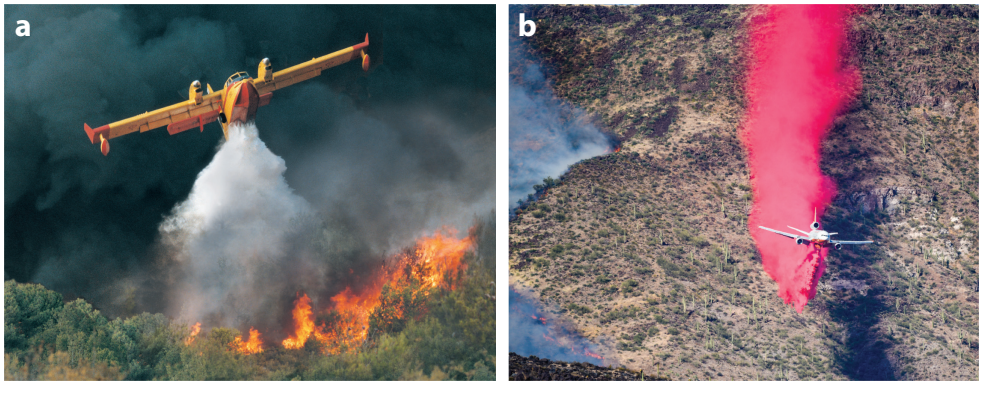

Figure 1

The two strategies used to fight fires with an airtanker: (*a*) direct attack and (*b*) retardant barrier. (*a*) Direct attack: A Canadair CL-415 airtanker drops water directly on a fire. Photo provided by Viking Air Ltd. (*b*) Retardant barrier: A DC-10 (Air Tanker 914) drops retardant ahead of the advancing fire front in Arizona (June 20, 2020). Photo provided by JDH Images (**https://www.jdhimg.com/centralfire/**).

(AFF). The closest situation studied in the literature is the atomization of millimetric liquid jets injected transversally into subsonic gaseous cross flows, which are studied mostly for combustion applications (Broumand & Birouk 2016). An impressive number of correlations have been proposed for the liquid jet penetration and expansion and the column breakup point (No 2015, Rouaix et al. 2023), and different models have been developed to describe the liquid jet atomization process (Mashayek & Ashgriz 2011). The problem of rainfall retention by vegetation is also well studied and has several applications, such as agricultural spraying (Makhnenko et al. 2012) and painting (Wilson et al. 2018), which have a similar objective to deliver a uniform distribution of the product on the target substrate. Controlling the overall droplet size distribution is of importance. The challenge is to find an optimal size that is small enough to provide good deposition and coverage without being so small as to result in significant spray drift and evaporation. In these situations, the liquid is sprayed at a distance less than one meter and the mean droplet size is around 100 μm, which is almost two orders of magnitude smaller than the spraying process of an airtanker.

Aerial firefighting (AFF): the use of airtankers to fight fires

Some attempts to provide a global description of the liquid evolution after being dropped can be found in the literature, considering experiments at a reduced scale in wind tunnel (Satoh et al. 2000, Ito et al. 2010) and numerical simulations at the aircraft scale (Satoh et al. 2000, Rimbert 2003, Rouaix et al. 2023, Tomé 2004, Ito et al. 2010, Zhao et al. 2018, Calbrix et al. 2023), or by coupling models to describe the different phases of the liquid evolution between the airtanker and the ground (George & Johnson 1990; Amorim 2011a,b; Qureshi & Altman 2018).

This review provides an overview of the fluid dynamics of airtanker firefighting, a spectacular process displaying rich and varied physical phenomena. Most of these phenomena have been intensively investigated in different contexts and conditions, so the main results are collected and discussed here in order to provide a unified description of the process of delivering liquid dropped by an airplane onto vegetation.

1.2. Description of the Dropping Process

The review follows the series of events experienced by the dropped liquid as depicted in **Figure 2**: (①, liquid ejection) A liquid stored in a tank located inside the aircraft or under the fuselage is ejected at a liquid flow rate selected by the pilot; (②, liquid column penetration) a

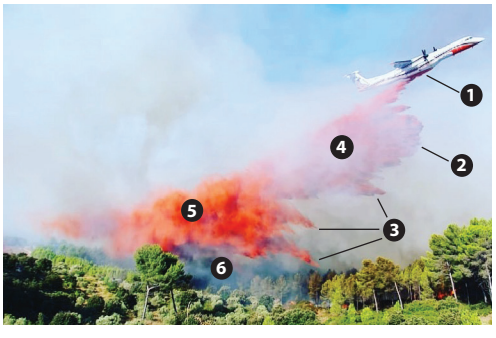

Figure 2

A Dash-8 airtanker from the French Civil Protection dropping 10 tons of retardant, illustrating the different phases of the liquid evolution from the airtanker to the ground: (①) liquid ejection from the aircraft, (②) liquid column penetration, (③) large-scale column fragmentation, (④) column surface atomization, (⑤) rainfall, and (⑥) liquid interception by vegetation. Photo adapted with permission from Centre d'Essais et de Recherche, Valabre, France.

liquid column develops under the aircraft that is shaped by the interaction with the air; (③, large-scale column fragmentation) a multimodal Rayleigh–Taylor-type instability develops with liquid spikes that can be observed on the front of the liquid column; (④, column surface atomization) an intense surface shear breakup process occurs, resulting in the production of a dense droplet cloud; (⑤, rainfall) the resulting liquid cloud interacts with the ambient air, which is presumably hot, windy, and turbulent; and (⑥, liquid interception) the droplets impact the vegetation and can spread, bounce, splash, levitate, run off the vegetation, or evaporate. All of these phenomena contribute to the overall retention efficiency.

2. PROBLEM STATEMENT: NONDIMENSIONAL NUMBERS

When addressing such a complex problem controlled by a large number of parameters and involving a rich variety of physical phenomena, the identification of the relevant nondimensional parameters is of key importance.

2.1. List of Parameters and Orders of Magnitude

The main parameters are shown in **Figure 3** and the problem may be described as the following. Over a period of time T, an airtanker at horizontal velocity U_a and at a constant altitude H is dropping a liquid (water or retardant) of density ρ_L, dynamic viscosity μ_L, and temperature T_L at velocity U_L into air of density ρ_a, dynamic viscosity μ_a, and temperature T_a under a wind of velocity W. The air–liquid surface tension is σ. The atomization process results in a size distribution $N(d)$ of droplets of size d and velocity v_d that finally settle and impact on the ground due to gravity, g. The substrate (leaf, wood, etc.) has a temperature T_S with wetting properties given by advancing and receding contact angles—θ_A and θ_R, respectively. The substrate is inclined, making an angle α with the horizontal. It is potentially rough or porous, with properties specified below as necessary.

To start, we should specify the order of magnitude of some important input parameters. The airtanker is dropping at a velocity $U_a \sim 50$–70 m/s a volume of 1–70 m^3 through a delivery system with an exit section of width $D \sim 0.3$–1 m and length $L \sim 1$–10 m with an exit velocity

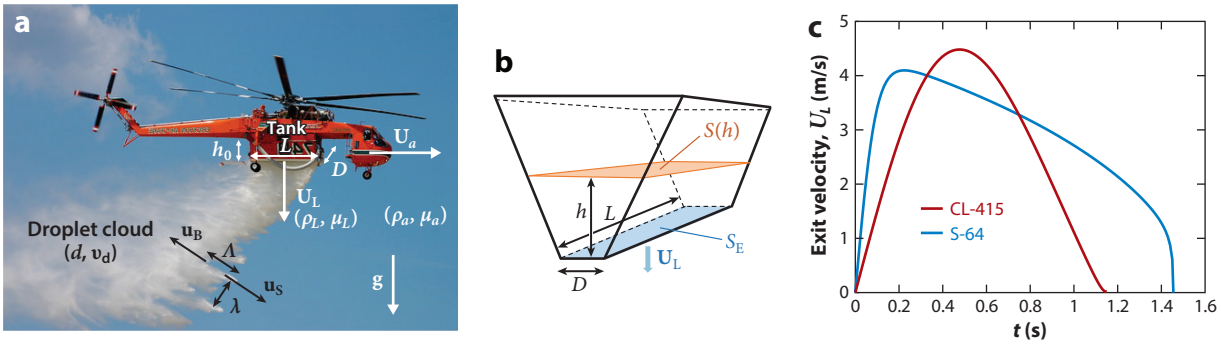

Figure 3

(*a*) Definition of the problem and its main parameters specified in the frame of reference moving with the airtanker (here an S-64 Aircrane helicopter): An airtanker drops a liquid of density ρ_L and dynamic viscosity μ_L at exit velocity U_L into air of density ρ_a and dynamic viscosity μ_a from height H. It results in a cloud of droplets of diameter d and velocity v_d, as well as in the development on the liquid column front of a large-scale instability of wave length λ, amplitude Λ, with liquid spike velocity u_S and air velocity penetration u_B. (*b*) Typical airtanker reservoir design, illustrating the contraction of the section $S(h)$ from the top to the exit opening. The height of liquid in the reservoir is Λ, and $S(h)$ and S_E are the area of the free surface and exit, respectively. (*c*) Typical exit velocities U_L for the liquid discharge from Canadair CL-415 (6 m^3) and S-64 Aircrane (30 m^3) airtankers at maximum opening. Photo copyright 2010 Nick Schweitzer; adapted with permission.

FIRE RETARDANT

Fire retardant is used to stop or reduce fire propagation. The retardant products currently in use, namely, Fire-Trol 931 in Europe and Phos-Chek in the United States, contain large amounts of fertilizer materials (the active fire retardant ingredient) such as ammonium sulfate and ammonium phosphates. These materials suppress fires by altering the pyrolysis products formed when the fuel is heated. They cause the material to undergo the production of a relatively thick char layer, reducing both the production of combustible volatiles and the rate of heat conduction into the material (Anderson et al. 1974, Pappa et al. 1995). Additional ingredients in small quantities (some percents in mass) are added: Retardants are thickened using gum and clay and colored to visualize the drop, and a corrosion inhibitor is added. They are manufactured as dry powders or as concentrated liquids that are diluted with water prior to use.

Detailed rheological characterizations of Fire-Trol 931 and Phos-Chek have been provided by Anderson et al. (1974) and Rimbert (2003). When diluted with water, the retardant mixture has a density of $\rho_L \sim 1{,}050$ kg/m^3, a surface tension of $\sigma \sim 0.04$ N/m and a viscosity of μ_L ranging from 0.05 to 0.6 Pa·s. The retardant has a complex non-Newtonian rheology combining shear-thinning and viscoelastic behaviors.

The main non-Newtonian property is related to a shear-thickening behavior that can be described using a power law relation for the apparent viscosity:

$$\mu_L = kD^{n-1}, \qquad \text{SB1.}$$

where D is the shear rate, k (in Pa·s^n) is the consistency, and n is the fluid index, which is lower than 1 for shear-thinning fluids. The value of n is found to significantly decrease with an increase in the mass concentration of gum—typically from $n = 0.85$ to $n = 0.36$ for 0.5% to 2% concentration in mass (Rimbert 2003).

The fluid elasticity is enhanced when increasing the concentration of gum and is mostly observed during rapid shear. Rimbert (2003) suggested describing the viscoelasticity property of Fire-Trol 931 using a Maxwell–Jeffreys model, while Anderson et al. (1974) proposed using for all retardants an apparent viscosity $\mu_L(D)$ correlated to the shear rate D, which incorporates both viscous and elastic effects.

The shear-thinning properties guarantee an efficient discharge from the tank and improve liquid surface atomization, while the high viscosity combined with the viscoelastic property maximizes the final droplet size (reducing dispersion and evaporation losses) and increases fuel retention by the canopy.

$U_L \sim 2$–10 m/s at an altitude around $H \sim 50$ m. The resulting drop duration is $T \sim 2$–10 s. The dropped liquid can be water or a fire retardant (see the sidebar titled Fire Retardant). The retardant density is close to the water density $\approx$1,050 kg/m^3; its viscosity can vary from 50 to 600 times the water viscosity and it has non-Newtonian viscoelastic and shear-thinning properties. The atomization process results in the production of droplets of size 10 μm–1 cm that deposit on the ground to form a ground pattern of length $L_G \sim U_a T \approx 100$–$700$ m, width $\lambda_G \sim 50$ m, and maximum liquid concentration along the drop pattern centerline $\eta_{max} \sim 1$–4 L/m^2.

2.2. Nondimensional Numbers

Fire retardant: a non-Newtonian liquid mixture used to reduce or stop the spreading of fires

Classically, the liquid atomization process in an air flow is controlled by liquid and gas Reynolds numbers (the ratio of inertial to viscous forces), liquid and gas Weber numbers (the ratio of inertial to capillary forces), and the Ohnesorge number (the ratio of the viscous timescale to the capillary timescale). The liquid column Reynolds number is $Re_L = \rho_L U_L D/\mu_L \sim 10^4$ to 10^5 for retardant and $Re_L \sim 5 \times 10^6$ for water; the air Reynolds number is $Re_a = \rho_a U_a D/\mu_a \sim 5 \times 10^6$. These values indicate highly turbulent flows for both the liquid jet and the displaced air motion. The liquid Weber number is $We_L = \rho_a U_L^2 D/\sigma \sim 5 \times 10^5$ and the air Weber number is

$We_a = \rho_a U_a^2 D/\sigma \sim 10^5$, both of which are more than two orders of magnitude larger than those considered for the atomization of millimetric liquid jets injected in cross flow (Rouaix et al. 2023). Their values indicate an intense breakup process. Finally, the Ohnesorge number is $Oh = \mu_L/\sqrt{\rho_L \sigma d} \sim 0.25$ for the retardant; this is much larger than $Oh \sim 4 \times 10^{-3}$ for water. The values given here are for droplets of diameter $d = 1$ mm, and this important difference in the value of Oh is the consequence of a higher viscosity for the retardant.

The specificity of this problem comes from the similar orders of magnitude of the liquid inertia at ejection, the air inertia impacting the liquid column, and the liquid gravity acceleration,

$$\rho_L g D \sim \rho_L U_L^2 \sim \rho_a U_a^2, \tag{1.}$$

which results in two nondimensional numbers of order $\mathcal{O}(0.1 - 10)$ for the description of the liquid penetration: the momentum ratio $q = \rho_L U_L^2/\rho_a U_a^2$ (the ratio of liquid to air kinetic energy) and the Richardson number $Ri = gD/U_L^2$ (the ratio of gravity to inertia). Depending on the operating condition (U_L and U_a) and the delivery system (length L and width D), the value of the group (q, Ri) determines the column penetration, as discussed in the next section.

3. LIQUID EJECTION

Each airtanker has its own delivery system. The tank can be located inside the aircraft, as in the Canadair CL-415 (see **Figure 1*a***), or under the fuselage along the centerline of the aircraft's belly, as in the DC-10 shown in **Figure 1*b*** and the Dash-8 in **Figure 2**. The main objective is to deliver liquid at a constant and controlled flow rate to reach the needed performance on the ground. The pilot selects on the control panel the coverage levels in fixed steps, indicated by the values starting from 1 up to 8 for the most efficient systems. These values are in units of US gallons per 100 square feet of horizontal surface (GPC). A "full salvo" or "full load" drop is usually available to select the maximum drop-door aperture to provide the maximum load. Translated to metric units, the indicated coverage level values of 1–8 GPC are equivalent to about 0.4–3.2 L/m^2, respectively. In practice, the selected coverage level settings are less than 6 for light fuels such as grasslands, between 6 and 8 for fires in eucalyptus forests and up to 8 and "full load" for high-intensity fires and in areas with high fuel loads.

3.1. Tank Discharge

A representative design of an efficient reservoir is shown in **Figure 3*b*** and corresponds to, for example, one of the three central tanks under the DC-10 belly, the tank of the S-64 Aircrane helicopter (see **Figure 3**), or the Retardant Aerial Delivery System inside the C-130 Hercules. The tank design is characterized by the aspect ratio $\chi = L/D$ and the evolution of the area of the free surface $S(h)$ is characterized as a function of the height in the reservoir h. As shown below, the exit velocity is controlled by the function $S(h)$. By integrating the Euler equation along a streamline connecting the free surface of the liquid to the exit, and representing the total pressure loss in the system using a unique loss factor K, we can give the evolution of the fluid velocity u along the streamline as

$$\int_S^E \rho \frac{\partial u}{\partial t} \mathrm{d}s + \int_S^E \frac{\partial}{\partial s}\left(P + \frac{1}{2}\rho u^2\right) \mathrm{d}s = \rho g h - K \frac{1}{2}\rho U_L^2. \tag{2.}$$

The equation satisfied by the exit velocity U_L as a function of the evolution of the liquid level h in the tank is $U_L(h) = (S(h)/S_E)\mathrm{d}h/\mathrm{d}t$, with $h(t)$ given by

$$\int_h^0 \frac{\partial}{\partial t}\left(\frac{S(h)}{S(s)}\frac{\mathrm{d}h}{\mathrm{d}t}\right)\mathrm{d}s + \frac{1}{2}\left(\frac{\mathrm{d}h}{\mathrm{d}t}\right)^2\left[\left(\frac{S(h)}{S_E}\right)^2(1+K) - 1\right] = \frac{P_R - P_E}{\rho} + gh. \tag{3.}$$

The reservoir is usually vented to the cabin pressure by a vent system installed on top of the tank to avoid any depression inside the tank so that we consider $P_R \approx P_E$. Some systems use tank pressurization to enhance the tank discharge, such as the Modular Airborne Fire Fighting System or the Boeing 747. However, due to pressurized air management, their design is different from the one shown in **Figure 3*b***, and this discussion does not apply to such systems. Note that in some situations, typically to successfully pass the certification requiring a certain concentration threshold on the ground, the cabin can be pressurized to have $P_R > P_E$, increasing the flow rate of the delivery system. From Equation 3, it is possible to estimate the maximum exit velocity $U_{L,max}$ as a function of the initial liquid height h_0 as

$$U_{L,max} \approx \left[\frac{2gh_0}{1 + K - (S_E/S(h_0))^2}\right]^{1/2}. \quad 4.$$

Considering that the main pressure loss results from the geometry contraction at the exit $K \approx 0.5$, and for a significant section reduction, $(S_E/S(h_0))^2 \ll 1$, as a first approximation the maximum velocity can be estimated as 80% of the Toricelli velocity $\sqrt{2gh_0}$. For $h_0 \approx 2$ m, a typical maximum exit velocity is $U_{L,max} \approx 5$ m/s. **Figure 3*c*** shows the exit velocity evolution obtained by solving Equation 3 with the appropriate function $S(h)$ for the Canadair CL-415 airtanker (6 m^3) and the S-64 Aircrane helicopter (10 m^3), both with the full-load setting, corresponding to the maximum exit surface area S_E. A nonconstant flow rate is observed from the evolution. In practice, when aiming to deposit uniform lines of retardant on the ground at a desired concentration, the exit section is varied over time, $S_E(t)$, to deliver a constant flow rate. Each step on the pilot control panel (from 1 to 8) is associated with a predefined door aperture function $S_E(t) = \psi DL$, where $\psi(h(t))$ is the level of opening of the tank door, as controlled by the system computer.

3.2. Liquid Penetration

Figure 4 reveals different shapes for the liquid penetration. This can be explained using simple trajectory modeling for predicting the liquid column shape just after its injection in the vertical plane (x, z), where x and z are the horizontal and vertical coordinates, respectively. We consider the motion of a volume element of the liquid column of vertical thickness e. Close to the injection the liquid column has not been significantly deformed, and in a first approximation its horizontal

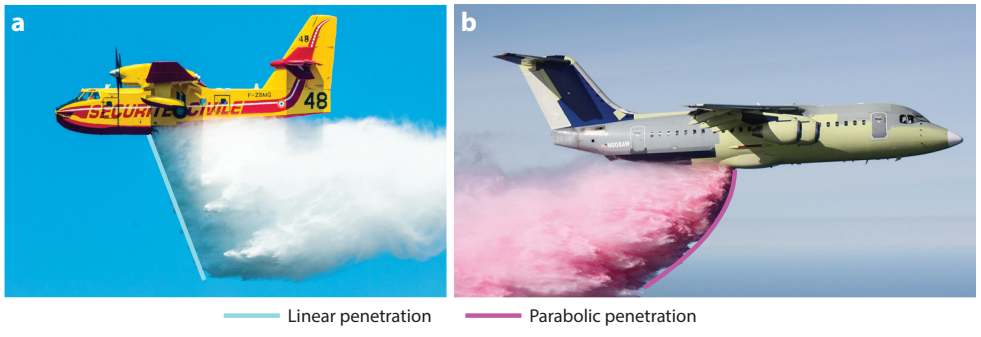

Figure 4

Penetration of the liquid after being released from (*a*) a Canadair CL-415 airtanker (with a capacity of 6 m^3), showing a linear penetration, and (*b*) a BAe-146 airtanker transformed by Tronos (with a capacity of 12 m^3), showing a parabolic penetration. Photographs provided by (*a*) Alain Franchi and (*b*) Tronosjet Maintenance Inc., reproduced with permission.

section is $S \approx D \times L = \psi \chi D^2$ with a constant level of opening ψ of the tank door. The horizontal deviation of the liquid column results from the drag force imposed by the impacting air,

$$\rho_L e S \frac{d^2x}{dt^2} \approx C_D \frac{1}{2} \rho_a D e U_a^2, \quad 5.$$

where C_D is the drag coefficient depending on the shape of the liquid column. When the liquid inertia is dominant compared to gravity ($Ri < 1$), the vertical motion of each element is imposed by the velocity of fluid release U_L as $dz/dt \approx U_L$ and the liquid column trajectory is then

$$x \approx C^* q \frac{z^2}{D}. \quad 6.$$

As shown, the penetration follows a parabolic profile and is controlled at first order by the aerodynamics of the liquid column, as characterized by $C^* = C_D/\psi\chi$ and the momentum ratio q. This evolution, also seen in the near field expansion of small liquid jets (Wu et al. 1997), is observed for dropping conditions controlled by the liquid inertia, as shown in **Figure 4*b***.

Let us now consider the situation where the liquid motion at the tank exit is driven by gravity ($Ri > 1$), the liquid column vertical motion is now $d^2z/dt^2 \approx g$, and the liquid column trajectory is

$$x \approx C^* Ri\, q z. \quad 7.$$

As shown, the penetration follows a linear evolution controlled by the nondimensional group $Ri\, q = \rho_L g D/\rho_a U_a^2$, which compares the liquid acceleration due to gravity to the air inertia impacting the liquid column. This linear evolution is consistent with the liquid column penetration of the Canadair CL-415 shown in **Figure 4*a***. Note that the Richardson number may vary during the drop because of the variation of U_L (see **Figure 3*c***), thus changing the penetration shape.

4. LARGE-SCALE COLUMN FRAGMENTATION

Supplemental Material >

Figures 2, **3**, and **5** (see also **Supplemental Video 1**) show the development of the liquid column. They reveal the presence of large-scale liquid spikes that move in a direction normal to the liquid column front. Comparing these figures also indicates that the number and size of the spikes seem to vary depending on the aircraft and the operating conditions.

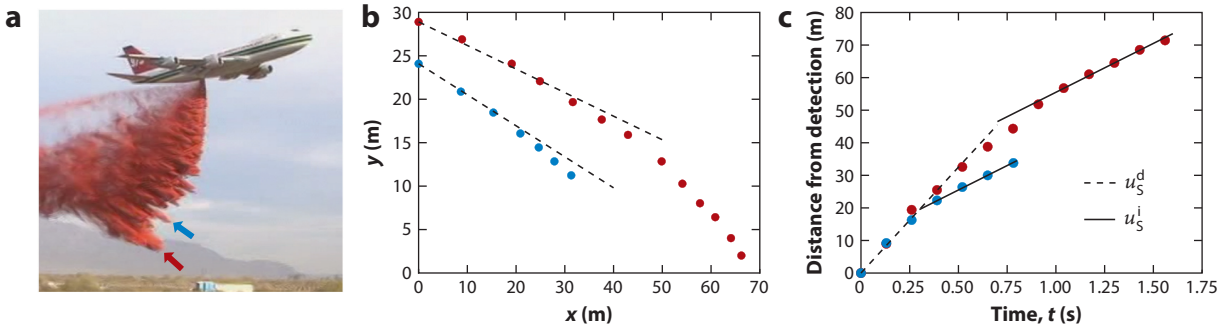

Figure 5

(*a*) Retardant dropped by a Boeing 747 developing large-scale structures of bubbles and spikes characteristic of the Rayleigh–Taylor instability. Image taken 3 s after the beginning of the drop process shown in **Supplemental Video 1**, which was used to create the plots in panels *b* and *c* (with permission of the US Forest Service). (*b*) Trajectory of the liquid spikes identified with corresponding colored arrows in panel *a*. The dashed line is to help the eyes follow a linear trajectory. (*c*) Distance from the spike detection as a function of time. The dashed line shows the velocity of the spikes $u_S^d \approx 0.9U_a$ when detected ($t = 0$), and the solid lines show the stabilized velocity before impact $u_S^i \approx 0.4U_a$, with U_a the airtanker velocity.

4.1. A Multimodal Rayleigh–Taylor Instability?

The observed behavior in a first attempt can be related to the Rayleigh–Taylor instability observed whenever two fluids of different densities are accelerated against the density gradients (Rayleigh 1883, Davies & Taylor 1950). The driving acceleration a along the density gradient direction can be due not only to the gravity component in the direction normal to the interface but also to the acceleration U^2/R_j induced by the curvature R_j of the liquid column. Three subsequent stages in the Rayleigh–Taylor instability evolution are commonly reported. The initial phase of exponential growth in perturbations is followed by a transition phase of bubble/spike formation, followed by a stage of asymptotic development of coherent structures of air bubbles penetrating the liquid and liquid spikes penetrating the air, as shown in **Figure 2**. The dynamics of the structure is typically governed by two independent length scales (see **Figure 3** for the parameter definitions): the amplitude Λ in the direction of acceleration a and the spatial period λ parallel to the interface. The scale λ is set by the mode of fastest growth or by the initial perturbation (Abarzhi 2008).

Initially some perturbations of wavelength λ at the liquid interface grow with time. From the linear theory of inviscid fluid the growth is exponential, $\Lambda \sim \lambda \exp(t/\tau)$, with the characteristic timescale $\tau = \sqrt{\lambda/g}$ (Rayleigh 1883). Considering the effect of the surface tension shows that the mode of fastest growth is close to the capillary length $\lambda_\sigma = (3\sigma/\rho_L a)^{1/2}$; considering viscosity only, the mode of fastest growth is $\lambda_\nu = \left(8\nu_L^2/a\right)^{1/3}$ with ν_L the kinematic viscosity. When considering both surface tension and viscosity, the effect of viscosity is to shift the mode of fastest growth to greater wavelengths compared to λ_σ (Bellman & Pennington 1954).

Here, the liquid–air surface perturbations have different origins: (*a*) the Kelvin–Helmholtz instabilities that form at the very beginning of development with wavelength $\lambda_{KH} \sim \sigma/\rho_a(\Delta u)^2$ due to the velocity jump Δu between the two phases and then, when the vorticity layer of thickness δ has developed, with wavelength $\lambda \sim \delta(\rho_L/\rho_a)^{1/2}$ (Marmottant & Villermaux 2004); (*b*) the large-scale flow and surface perturbation induced by the delivery system; and (*c*) the turbulence of the liquid column. The combination of all these sources of perturbation results in a multimodal Rayleigh–Taylor instability where large coherent structures develop through the competition between bubbles and spikes (Lewis 1950, Alon et al. 1995). The coupling of the tangential λ and normal Λ scales and the dependency on the initial perturbation spectra are still open problems to be addressed (Abarzhi 2008). What can be extrapolated from the abundant literature on the Rayleigh–Taylor instability to the airtanker large-scale liquid column fragmentation is explained below.

According to the exponential growth relation of the small perturbations, short wavelengths grow more rapidly than long wavelengths. Then, when the amplitude of the perturbation becomes significant compared to the wavelength, the penetration velocity of the spikes u_S into the air can be proposed by considering the balance between the penetrating liquid volume V at acceleration a and the drag force experienced by the spike as $\rho_a u_S^2 S \approx \rho_L a V$, where S is the spike front area. Considering $V/S \sim \lambda$, the spike velocity is given by $u_S \sim \sqrt{a\lambda}$. Thus, short-wavelength perturbations grow more slowly than long-wavelength perturbations. Similar arguments apply to the velocity penetration of the bubbles inside the liquid. The result of this behavior is that one expects small structures to appear first on the liquid column front close to the ejection, and then as time proceeds, larger structures dominate the front evolution, as observed far from the exit (see **Figures 3** and **5**). When the initial condition has been forgotten, at^2 is the only dimensional length scale of the problem; and both bubble and spike fronts grow as at^2 and exhibit a self-similar behavior with this scale (Alon et al. 1995). As a consequence, the spikes and bubbles formed in the airtanker liquid column are expected to evolve as $\lambda \sim at^2$, $\Lambda \sim at^2$, and $u_S \sim at$.

4.2. Ejection of Liquid Meteors

Supplemental Material >

The available videos made during airtanker qualification testing using the cup-and-grid method (see **Supplemental Video 1**) are not sufficiently accurate in both time and space to observe the first stage of the multimodal Rayleigh–Taylor development. What is clearly observed is the formation of liquid spikes developing all along the dropping process, as also seen in **Figure 5**. **Supplemental Video 1** shows a Boeing 747 dropping 30 m^3 of retardant in $T = 4$ s at a velocity of $U_a = 69$ m/s and altitude of $H = 67$ m. The video clearly reveals a large number of spikes evolving from the liquid column front. Once detached, they seem to travel along a rectilinear path while being progressively atomized by shear surface breakup, similar to meteors in the atmosphere. Different spikes are identified and tracked during their evolution. The parallax changes during the video, and it has been roughly corrected by tracking the evolution of the airtanker length. The trajectories of several spikes are shown in **Figure 5*b***, and the time evolution of the distance from the onset of their detection is shown in **Figure 5*c***. The spikes' trajectories clearly start with a rectilinear motion before deviating due to gravity and impacting the ground at an oblique angle. In this situation, the motion is characterized by two distinct velocities. The velocity at detachment from the column front is $u_S^d \approx 0.9U_a$ and the spikes impact the ground at a velocity $u_S^i \approx 0.4U_a$. Both velocities have an order of magnitude similar to U_a, the horizontal liquid velocity at injection into the air.

5. COLUMN SURFACE BREAKUP

When a liquid–air interface experiences an intense shear, the interface is destabilized, giving birth to liquid breakup and the production of droplets. This breakup mechanism has been extensively investigated for pipe flow (Kataoka et al. 1983), liquid jet injection in cocurrent flow (Marmottant & Villermaux 2004) or cross flow (Broumand & Birouk 2016), agricultural-like sprays (Vallon et al. 2021), and the sea surface (Veron 2015). These different applications differ mostly by their geometry and operating conditions (i.e., air and liquid velocity and induced shear), but they have in common similar physical phenomena controlling the produced droplet size distribution.

5.1. Breakup Mechanism

The shear surface breakup mechanism originates in the development of a Kelvin–Helmholtz-type instability. Surface perturbations are amplified because of a pressure decrease at the crests, while pressure is increased in the troughs, resulting in aspiration and compression effects, respectively. The description is made in the reference frame moving with the aircraft (see **Figure 3**). The liquid of velocity $U_L e_z$ is interacting with a relative air flow of velocity $-U_a e_x$. With typical values of $U_L \approx 5$ m/s and $U_a \approx 70$ m/s, the relative interface shear is characterized by the velocity jump across the interface $\Delta u \approx U_a$ with an inclination angle $\theta \approx U_L/U_a$ less than 10° above the horizontal. Considering the Reynolds number involved here ($Re_a = DU_a/\nu_a \approx 5 \times 10^5$), a turbulent boundary layer develops on the liquid surface with a velocity gradient $dU_a/d\eta = u_*^2/\nu_a$, where η is the coordinate normal to the interface and ν_a is the kinematic viscosity of air. The vorticity layer thickness in the air is $\delta = U_a/(dU_a/d\eta) = U_a\nu_a/u_*^2$. Given $u_* \approx 1$ m/s, we have $\delta \approx \nu_a U_a/u_*^2 \approx 1$ mm. A thin vorticity boundary layer of size δ develops, and the most amplified wavelength is $\lambda \sim \delta(\rho_L/\rho_a)^{1/2}$ since we have $We_\delta = \rho_a(\Delta u)^2\delta/\sigma > (\rho_a/\rho_L)^{1/2}$ (Villermaux 2020). Compared to the liquid column size $D \sim 1$ m, λ/D is much less than 1 and the problem is similar to a plane interface subjected to a high shear, as observed for such high air velocities in the formation of sea sprays (Troitskaya et al. 2018). In such conditions, the Kelvin–Helmholtz instability at the air–water boundary leads to the development of both liquid ligaments (Koga 1981) and bags (Veron et al. 2012), both of which break into droplets, as illustrated in **Figure 6**.

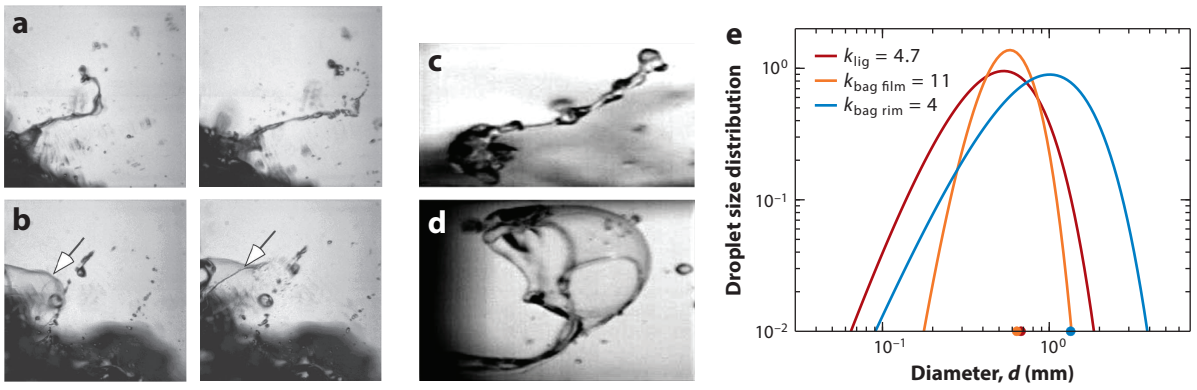

Figure 6

(*a*,*b*) Ligament (*a*) and bag (*b*) breakups observed at a sheared liquid surface in a wind wave tank (*arrows* show a bag formed by the airflow). Panels *a* and *b* reprinted with permission from Veron et al. (2012). (*c*,*d*) Ligament (*c*) and bag (*d*) breakups observed at the surface of a water film in a horizontal pipe flow. Panels *c* and *d* reprinted with permission from Boulesteix (2010). (*e*) Comparison of the water droplet distributions produced by a ligament and a bag (film and rim). The dots on the *x*-axis are the corresponding mean diameters. k_{lig}, $k_{bag\,film}$ and $k_{bag\,rim}$ are the order of the Gamma distribution for droplet generation by ligament, bag film, and bag rim, respectively. *d* is the droplet diameter.

Different size distribution expressions have been proposed to describe the droplet population produced by breakup events (Villermaux 2007, Rimbert & Castanet 2011, Vallon et al. 2021). In the following, the distributions of droplets produced by bag or ligament breakup will be represented using the Gamma distribution of order *k*,

$$\mathcal{P}_k(x) = \frac{k^k}{\Gamma(k)} x^{k-1} e^{-kx}, \qquad 8.$$

where $\Gamma(k) = \int_0^{+\infty} x^{k-1}\, e^{-x} \mathrm{d}x$ is the Gamma function. This distribution has been shown to well reproduce experiments reporting breaking mechanisms at sheared interfaces and it is often used in the development of sea spray droplet distribution modeling (Mueller & Veron 2009, Veron 2015, Troitskaya et al. 2018, Deike 2022).

5.2. Ligament Breakup

Liquid acceleration at the crest of the surface perturbation results in ligament formation, elongation, and breakup. Based on experiments on a round liquid jet 7.8 mm in diameter destabilized by a coaxial fast airstream varying from 19 to 59 m/s, Marmottant & Villermaux (2004) reported a detailed inspection of the ligament formation, deformation, and breakup. The dynamics of the ligaments is related to the development of a transverse instability, $\lambda_\perp \simeq 3\lambda We_\lambda^{-1/3} \simeq 3\delta We_\delta^{-1/3} (\rho_a/\rho_L)^{-1/3}$ (with $We_\lambda = \rho_a U_a^2 \lambda/\sigma$), and produces ligaments of mean equivalent diameter $\langle D_{eq}\rangle \simeq 0.23\lambda_\perp$, length independent of the air velocity $L_\ell \sim U_a^0$, and thickness $\xi_\ell \sim U_a^{-3/2}$. Each ligament breakup produces droplets of different sizes larger than the mother ligament thickness, ξ_ℓ. The average droplet size is $\langle d_{lig}\rangle = 0.4 D_{eq}$, which corresponds to an average number of $n_{d/lig} = 15.6$ droplets produced per ligament. The distribution of the normalized droplet size $q_{lig}(x = d/D_{eq})$ can be well represented using the Gamma distribution (Equation 8) of order *k*, $q_{lig}(x) = \mathcal{P}_k(x)$ with $k = k_{lig} \approx \langle d_{lig}\rangle/\xi_\ell$. From these results, we show in **Figure 6*e*** a size distribution for water droplets produced by ligament breakup in conditions relevant for an airtanker drop.

Increasing the viscosity with a glycerol solution, Marmottant & Villermaux (2004) reported more elongated ligaments that are thinner in diameter and thus break into smaller droplets. The effect of a viscoelastic property was addressed in the experiments of Keshavarz et al. (2015, 2016). The viscoelasticity monotonically increases the average droplet size $\langle d_{\rm lig}\rangle$ with a linear dependency on $\ln(De_{R_\ell})$, where the Deborah number, $De_{R_\ell} = \tau_{\rm E}/\sqrt{\rho R_\ell^3/\sigma}$, is defined in terms of $\tau_{\rm E}$, the characteristic relaxation time for the viscoelastic liquid. The droplet distribution is then described by a Gamma distribution with $k = 4$, and $R_\ell = D_{\rm eq}/2$.

5.3. Bag Breakup

The bag formation also originates in the liquid surface perturbation by a Kelvin–Helmholtz instability. The amplified perturbation is transformed into a bag that expands and then breaks. The bag breakup phenomenon has been identified to be of significant importance in the surface shear breakup mechanism (Veron et al. 2012, Troitskaya et al. 2018). The droplet production scenario proposed by Troitskaya et al. (2018), which is based on a bubble bursting at a surface, is adapted here. The bag is decomposed into a thin-film cap called the bubble delimited by a thick rim forming a toroidal ligament. The process of bag breakup is then the combination of, first, the film breakup at radius $R_{\rm b}$ through the development of a Rayleigh–Taylor instability, followed by the rupture of the toroidal ligament by capillarity. As a result, the size distribution of droplets shows two modes. The ratio of the rim volume to the initial droplet volume satisfies $V_{\rm r}/V_0 \approx 0.56$ and is independent of the Ohnesorge number Oh (Chou & Faeth 1998). Troitskaya et al. (2018) observed the bag size $R_{\rm b}$ at breakup to expand as u_*^{-1} (their data are fitted by $R_{\rm b} \approx 0.0096 u_*^{-1}$). The fragmentation was observed for the film thickness $h_{\rm b} = R_{\rm b}^2/\mathcal{L}$, with $\mathcal{L} = \ell_{\rm ac}/\epsilon^{1/2}$, where $\epsilon^{1/2} \approx 1.35 \times 10^{-4}$ is the puncture efficiency factor (Lhuissier & Villermaux 2012) and $\ell_{\rm ac} = \sqrt{\sigma/\rho_{\rm L} a_{\rm c}}$ is a capillary length based on the film acceleration $a_{\rm c}$ during the bag expansion. Compared to the case of a bubble bursting under gravity, the acceleration $a_{\rm c}$ should be taken here as the acceleration at the crest of the surface perturbation, $a_{\rm c} = \rho_{\rm a} U_{\rm a}^2/\rho_{\rm L}\lambda_\perp$ (Marmottant & Villermaux 2004), and not g, as used by Troitskaya et al. (2018). The film breakup generates a droplet diameter distribution $q_{\rm film}(x = d/\langle d_{\rm film}\rangle)$ following the Gamma distribution (from Equation 8) with $k = k_{\rm film} = 11$. The average droplet diameter generated by the burst of the bag film is $\langle d_{\rm film}\rangle \simeq 2R_{\rm b}^{3/8} h^{5/8}$, and the total number of droplets is $n_{\rm d/film} \simeq (R_{\rm b}/\ell_{\rm ac})^2 (R_{\rm b}/h_{\rm b})^{7/8}$. At the moment of rupture, the liquid ring has a thickness $\xi_{\rm rim} \simeq 0.065 R_{\rm b}$, and its fragmentation follows the ligament breakup mechanism described above. By subtracting the film volume, we can determine that its equivalent diameter is $D_{\rm rim} = 0.34 R_{\rm b}$, generating an average number of droplets per bag of $n_{d/{\rm rim}} = 8.3$ of mean diameter $\langle d_{\rm rim}\rangle = 0.4 D_{\rm rim} = 0.14 R_{\rm b}$. The droplet distribution diameter is then described with the Gamma distribution $\mathcal{P}_k(x = d/\langle d_{\rm rim}\rangle)$ (Equation 8) with $k = k_{\rm rim} = 4$. The resulting water droplet distributions produced by the rupture of both the film and the rim, in conditions relevant for an airtanker drop, are compared in **Figure 6*e*** to the droplet distribution generated by ligament breakup.

5.4. Toward an Airtanker Spray Generation Function

Providing a predictive description of liquid column atomization in airtanker firefighting appears very challenging considering the complexity of the process (see the sidebar titled The Process of Airtanker Spraying). The first step proposed here consists of defining a spray generation function, following the approach developed for ocean spray, by considering the predominance of ligament breakup (Mueller & Veron 2009), bursting bubbles (Veron 2015, Deike 2022), or bag breakup (Troitskaya et al. 2018). The airtanker spray generation function (ASGF) $\mathcal{F}(d)$ is defined as the number of droplets of diameter d generated per unit surface column area per unit time. For such an approach, a key issue, still to be investigated, is the evolution of the area of the surface of the liquid

THE PROCESS OF AIRTANKER SPRAYING

The liquid column formed under the airtanker penetrates the air, showing a linear or parabolic shape. The liquid column is subject to an intense surface shear breakup mechanism, presumably through the formation of both ligaments and bags, resulting in a multimodal distribution of droplet sizes. At the liquid column front, a large-scale Rayleigh–Taylor-type instability develops, resulting in the formation of liquid spikes that move, similar to meteors penetrating the atmosphere, in an oblique direction toward the ground at a velocity close to that of the airtanker. These liquid meteors are also subject to an intense surface breakup mechanism. The development of the large-scale instability increases the surface of the liquid phase, making the breakup process more efficient, but also depositing the liquid on the ground nonuniformly.

column. For sea applications, the wavy surface is clearly defined, while during the atomization of the dropped liquid the surface of the liquid column evolves in time and significantly varies due to the development of the large-scale fragmentation process.

Considering that both ligament and bag breakup events control liquid atomization, $\mathcal{F}(d)$ has to be built on the size spectra of droplets produced per ligament and bag combined with the frequency distribution (per unit surface, per unit time) of ligament $q_{\text{lig}}(D_{\text{eq}})$ and bag $q_{\text{bag}}(R_{\text{b}})$ size, represented by their equivalent diameter D_{eq} and radius R_{b}, respectively. The size spectrum of droplets produced by a ligament of equivalent diameter D_{eq} is then

$$F_{\text{lig}}(d, D_{\text{eq}}) = \frac{n_{\text{d/lig}}}{\langle d_{\text{lig}} \rangle} \mathcal{P}_{k_{\text{lig}}} \left(\frac{d}{\langle d_{\text{lig}} \rangle} \right), \qquad 9.$$

while the size spectrum of droplets produced by a bag of radius R_{b} is the sum of the film and rim contributions:

$$F_{\text{bag}}(d, R_{\text{b}}) = \frac{n_{\text{d/film}}}{\langle d_{\text{film}} \rangle} \mathcal{P}_{k_{\text{film}}} \left(\frac{d}{\langle d_{\text{film}} \rangle} \right) + \frac{n_{\text{d/rim}}}{\langle d_{\text{rim}} \rangle} \mathcal{P}_{k_{\text{rim}}} \left(\frac{d}{\langle d_{\text{rim}} \rangle} \right). \qquad 10.$$

The resulting ASGF is then

$$\mathcal{F}(d) = \int_{\text{bag}} q_{\text{bag}}(R_{\text{b}})\, F_{\text{bag}}(d, R_{\text{b}})\, \mathrm{d}R_{\text{b}} + \int_{\text{lig}} q_{\text{lig}}(D_{\text{eq}})\, F_{\text{lig}}(d, D_{\text{eq}})\, \mathrm{d}D_{\text{eq}}. \qquad 11.$$

The frequency distribution of bag size has been reported by Troitskaya et al. (2018) to follow a Gamma distribution, $q_{\text{bag}}(R_{\text{b}}) = \langle N_{\text{bag}} \rangle / \langle R_{\text{b}} \rangle \mathcal{P}_{k_{\text{bag}}}(R_{\text{b}}/\langle R_{\text{b}} \rangle)$, with $k_{\text{bag}} = 7.53$, where the mean number of bag events per unit surface per unit time $\langle N_{\text{bag}} \rangle$ increases with the friction velocity as $\langle N_{\text{bag}} \rangle = N_0 u_*^2 / U_0^2 \exp\left(-U_0^2/u_*^2\right)$, where $N_0 = 4.6 \times 10^2$ m^{-2}s^{-1} and $U_0 = 2$ m/s were obtained by fitting their experimental data.

To go further in the development of the ASGF, one needs to include important missing elements such as the frequency distribution of ligaments and the evolution of the liquid column surface area. In addition, the collected information on bag and breakup mechanisms in this review must all be confirmed under the conditions of atomization of the airtanker liquid column.

6. IN THE CLOUD

After their ejection from the liquid column surface, the droplets form a dynamic liquid cloud that penetrates a potentially hot and windy ambient air. The following discussion is based on the range of droplet diameters reported in **Figure 6*e*** that result from ligament and bag breakup.

6.1. Droplet Dynamics and Wind Dispersion

After their production at the liquid column surface, the droplets interact with the surrounding air velocity field $\mathbf{u}_a$ and settle due to the gravity field $\mathbf{g}$. The local air motion $\mathbf{u}_a$ is a priori complex because it results from the interaction between the large-scale structures induced by the liquid column wake and the air displaced by the development of the large-scale Rayleigh–Taylor bubbles inside the liquid column, with a possible contribution of wind velocity W. The motion of a spherical droplet of mass m_d and velocity $\mathbf{v}_d$ can be described in a first approach by considering the equation of motion [see Gatignol (1983) and Maxey & Riley (1983), as well as Veron (2015) for ocean spray and Shaw (2003) for atmospheric clouds]:

$$m_d \frac{d\mathbf{v}_d}{dt} = m_d\,\mathbf{g} + 3\pi\mu_a d f(Re_d)\,(\mathbf{u}_a - \mathbf{v}_d), \qquad 12.$$

where the inertial contribution from the ambient air (the pressure gradient and added mass), the lift force, and the Basset–Boussinesq history force are not considered. The function $f(Re_d) = \left(1 + 0.15Re_d^{0.687} + 0.0175Re_d/(1 + 4.24 \times 10^4\, Re_d^{1.16})\right)$ (Clift & Gauvin 1970) corrects the Stokes drag due to the inertia effect that appears when the droplet Reynolds number $Re_d = d \parallel \mathbf{u}_a - \mathbf{v}_d \parallel /\nu_a$ increases. The droplet response or relaxation time is $\tau_d = d^2\rho_L/(18\mu_a f(Re_d))$. Several τ_d after being generated, the droplet reaches its final velocity, $\mathbf{u}_a(\mathbf{x} = \mathbf{x}_d) + \mathbf{v}_{d,T}$, where $\mathbf{u}_a(\mathbf{x} = \mathbf{x}_d)$ is the air velocity at the droplet position $\mathbf{x}_d$ and $\mathbf{v}_{d,T}$ is the so-called droplet terminal velocity, whose magnitude $v_{d,T}$ is obtained by solving $v_{d,T} f(dv_{d,T}/\nu_a) = d^2\rho_L g/18\mu_a$. The evolution of the terminal velocity is shown in **Figure 7*a*** for water and fire retardant droplets. When the droplet size increases, it deforms, becoming flattened on the front and smoothly rounded on the rear, and exhibits oscillations (Testik & Barros 2007). The drag force thus increases and the terminal velocity decreases, with the curve in **Figure 7*a*** being then an upper limit for droplets with diameters larger than 1 mm. The comparison with the correlations usually considered for modeling droplets in rainfall (not shown in the figure for clarity) does not reveal any significant difference. The response of the droplet to the ambient air flow is usually characterized by the Stokes number $St_d = \tau_p/\tau_f$ where τ_f is a characteristic flow timescale. A value $St_d \ll 1$ indicates a tracer behavior, while $St_d \gg 1$ corresponds to a ballistic behavior not affected by the considered flow structure.

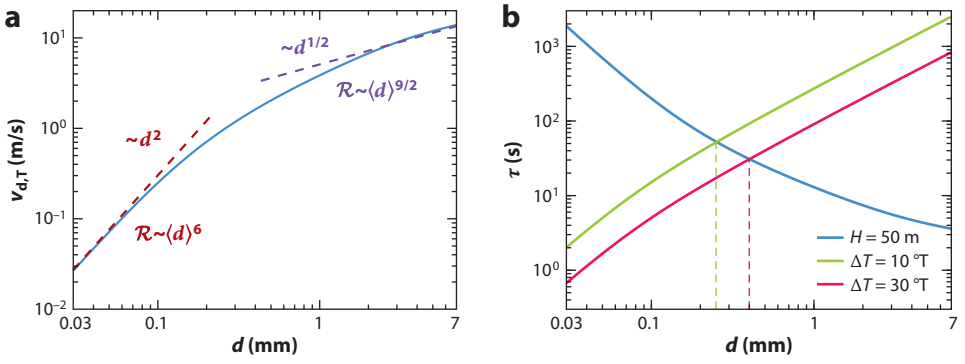

Figure 7

(*a*) Terminal velocity $v_{d,T}$ of a droplet (water and fire retardant) in the cloud as function of the droplet diameter d with the two asymptotic contributions to the rain rate $\mathcal{R}$. (*b*) Evaporation time of droplets for temperature differences $\Delta T = 10$°C and 30°C relative to the ambient air, compared to the settling time for droplets falling from a height of $H = 50$ m. Since the densities of water and fire retardant are very similar, a single curve is used to represent both liquids in panels *a* and *b*.

6.2. Droplet Evaporation

The liquid is dropped at the cabin temperature or at a temperature close to the temperature of the liquid when the tank is filled on the tarmac. The droplets will then most likely interact with dry air of a high temperature because the liquid is either directly dropped over the fire for a direct attack or in front of the fire propagation line for an indirect attack (see **Figure 1**). The situation thus differs notably from the ambient conditions of ocean spray (Veron 2015) and atmospheric clouds (Shaw 2003), where the ambient air is extremely humid and close to saturation. In the context of aerial firefighting, significant evaporation thus takes place, in particular, on the liquid cloud front that is continuously dried by the air it is penetrating. The droplet vaporization rate is given by

$$\frac{\mathrm{d}m_\mathrm{d}}{\mathrm{d}t} = -\pi d N u \lambda_\mathrm{a} \frac{T_\mathrm{a} - T_\mathrm{d}}{h_\mathrm{lv}}, \qquad 13.$$

where λ_a is the thermal conductivity in air, h_lv is the latent heat of vaporization, and T_d and T_a are the temperature of the droplet (assumed uniform) and the ambient air, respectively. The Nusselt number is $Nu = (2 + 0.57 Re_\mathrm{d}^{1/2} Pr^{1/3})/(1 + B_T)^{0.7}$ (Renksizbulut & Yuen 1983), with $Pr = \nu_\mathrm{a} \rho_\mathrm{a} C_\mathrm{p}/\lambda_\mathrm{a}$ the Prandtl number, $B_T = C_\mathrm{p}(T_\mathrm{a} - T_\mathrm{d})/h_\mathrm{v}$ the Spalding number, and C_p the specific heat of air. Integration of the vaporization rate equation gives the d^2 law,

$$d^2 = d_0^2 - 4 \frac{N u \lambda_\mathrm{a} (T_\mathrm{a} - T_\mathrm{d})}{\rho_\mathrm{L} h_\mathrm{v}} t, \qquad 14.$$

where $\tau_\mathrm{evap} \approx d_0^2 \rho_\mathrm{L} h_\mathrm{v}/4 N u \lambda_\mathrm{a} (T_\mathrm{a} - T_\mathrm{d})$ is an estimate of the droplet evaporation time and d_0 indicates the initial droplet diameter. The droplet evaporation time is reported in **Figure 7*b*** for different temperature differences $\Delta T = T_\mathrm{a} - T_\mathrm{d}$ and compared to the time required for the droplet to deposit on the ground for a typical height of $H = 50$ m. As shown, the evaporation can have a significant impact on the quantity of liquid that effectively deposits on the ground, but it mainly affects the droplets that are also dispersed by the wind. From **Figure 7*b***, one can see that the larger droplets need a few seconds to reach the ground while the smaller droplets in the cloud will need a half-hour—enough time to be evaporated or dispersed away with the wind.

6.3. Secondary Droplet Breakup

When moving in the air displaced by the liquid column and settling due to gravity, droplets can experience further breakup events (Rui 2024). Droplet breakup in air flow is described in terms of the maximum deformation that can support the droplet interface $\sim \sigma/d$ due to the inertia of the relative motion $\sim \rho \parallel \mathbf{u}_\mathrm{a} - \mathbf{v}_d \parallel^2 \approx \rho v_{\mathrm{d,T}}^2$ or the effect of the ambient turbulence $\sim \rho \overline{(\delta u)^2}$, where $\overline{(\delta u)^2}$ is the mean square velocity difference over a distance equal to the droplet scale. This results in two critical maximum Weber numbers (Hinze 1955, Pilch & Erdman 1987):

$$We_1 = \frac{\rho d_1 v_{d,\mathrm{T}}^2}{\sigma} = 12\,(1 + 1.077 Oh^{1.6}), \quad We_2 = \frac{\rho d_2\, \overline{(\delta u)^2}}{\sigma} = 1.18. \qquad 15.$$

When increasing the Ohnesorge number $Oh = \mu_\mathrm{L}/\sqrt{\rho_\mathrm{L} \sigma d}$, the expression for We_1 shows that breakup by inertia of the relative motion concerns droplets of larger diameter. Assuming an isotropic turbulence at the particle scale and that a particle diameter belongs to the inertial turbulent subrange, $\overline{(\delta u)^2}$ can be related to the dissipation rate ϵ as $\overline{(\delta u)^2} \approx 2\,(\epsilon d)^{2/3}$ (Hinze 1955). Considering the liquid column as a cylinder of diameter D, ϵ is roughly estimated here by considering the dissipation in the wake of a cylinder as $\epsilon \approx 0.12 \overline{U_0}^3/\overline{L_0}$, where $\overline{U_0}$ is the mean streamwise velocity on the centerline of the wake and $\overline{L_0}$ is the mean velocity half-width (Chen et al. 2018). At the distance $X = 10D$ in the wake, Chen et al. (2018) reported values of $\overline{U_0} \approx 0.22 U_\mathrm{a}$ and $\overline{L_0} \approx 0.66 D$. Equation 15 for We_1 and We_2 gives maximum droplet diameters for water of

$d_1 \approx 5$ mm and $d_2 \approx 1$ cm, respectively. When compared to the size distributions produced by bag and ligament breakup in **Figure 6*e***, no significant further atomization process is expected after the production of droplets at the liquid column surface.

6.4. Rainfall

During atmospheric rainfall, droplets can experience collisions resulting in bouncing, coalescence, or breakup (Testik & Barros 2007, Villermaux & Bossa 2010). The characterization of the droplet size distribution function $N(d)$ is of major importance for the prediction of precipitation. A widely accepted general form for $N(d)$ is (Steiner et al. 2004)

$$N(d) = N_0 d^{\mu} \exp(-\Lambda d), \qquad 16.$$

where N_0 [$\mathrm{m}^{-3}\ \mathrm{mm}^{-(1+\mu)}$] is the concentration scaling parameter, Λ (mm^{-1}) is the slope coefficient, and μ is the distribution shape factor. The rain rate $\mathcal{R}$ is then determined as

$$\mathcal{R} = \int N(d) \frac{\pi d^3}{6} v_{\mathrm{d,T}} \mathrm{d}d. \qquad 17.$$

The exponential raindrop size distribution ($\mu = 0$) is used here to show the impact of the droplet size on the airtanker rainfall. For large droplets, $v_{\mathrm{d,T}} \sim d^{1/2}$ entails $\mathcal{R} \sim \langle d \rangle^{9/2}$ (Villermaux & Bossa 2009), while for small droplets, $v_{\mathrm{d,T}} \sim d^2$ entails $\mathcal{R} \sim \langle d \rangle^6$.

It is speculative to directly extend the shape for $N(d)$ (Equation 16) observed for natural rainfall to the airtanker rainfall, for several major reasons: (*a*) The lifetime of the cloud is very short compared to atmospheric rainfall, (*b*) the atomization process of the liquid spikes ends tens of meters above the ground, and (*c*) the droplet concentration is heavily influenced by the large-scale fragmentation of the liquid column. This predictably results in a fully 3D and unsteady droplet size distribution, $N(x, y, z, t, d)$.

The effect of the retardant on the droplet size distribution was discussed by Tomé (2004), who considered experimental studies performed by the US Forest Service at the end of the 1970s. As expected, the particular rheology of the retardant (high viscosity combined with a viscoelastic behavior) resulted in droplets that were almost one order of magnitude larger than droplets generated with water. For example, at an aircraft speed of $U_a \approx 50$ m/s, water produces droplets with an average size around 1 mm, in agreement with **Figure 6*e***, while a Phos-Chek retardant solution produces droplets with an average diameter around 8 mm.

7. GROUND DEPOSITION

The droplets eventually deposit on the ground, where they form a line of protection against the fire. In this section, we first present the main characteristics of the resulting drop pattern, followed by a discussion of the physical mechanisms involved.

7.1. Deposition on a Flat Field Without Vegetation

The consideration of an airtanker's performance is necessary before it can be used to fight fires. This is typically evaluated by drop tests performed at realistic scales using the cup-and-grid method (Suter 2000), which involves collecting drops in cups (rain gauges) distributed in a grid on a flat field without vegetation. **Figure 8*a*,*b*** shows the drop pattern for two airtanker systems. Both systems provide regular deposition, but irregular distribution on the centerline can be observed as a direct consequence of the liquid spikes generated by the large-scale fragmentation of the liquid column.

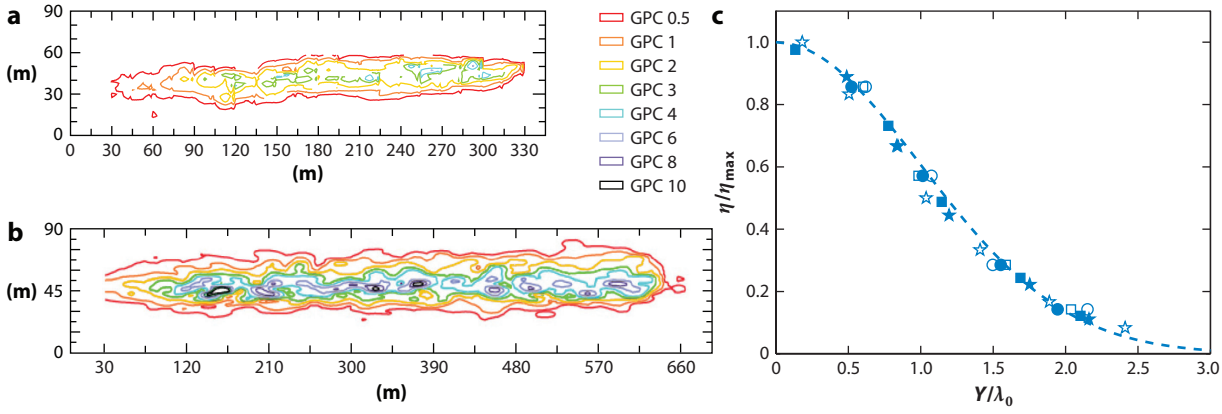

Figure 8

(*a*,*b*) Examples of drop patterns (Legendre et al. 2013) from (*a*) a CDF S-2T Turbo Tracker (dropped volume = 4.54 m^3) and (*b*) an Evergreen Boeing 747 (dropped volume = 68 m^3). The flight direction is from left to right. Each colored line represents an iso-concentration of product expressed in US gallons per 100 square feet of horizontal surface (GPC; 1 GPC ≈ 0.4 L/m^2). (*c*) Evolution of the normalized ground coverage η/η_{max} as a function of the transverse distance Y from centerline of the pattern, with λ_0 the standard deviation. Each symbol displays the mean width of a single drop. The white and blue stars are for the Evergreen Boeing 747 (*white star*: dropped volume = 32 m^3, altitude $H = 66$ m, $\eta_{max} = 1.8$ mm, $\lambda_0 = 24$ m; *blue star*: dropped volume = 29 m^3, altitude $H = 102$ m, $\eta_{max} = 2.4$ mm, $\lambda_0 = 34$ m), the white and blue circles are for the CDF S-2T Turbo Tracker (*white circle*: dropped volume = 4.6 m^3, altitude $H = 55$ m, $\eta_{max} = 1.4$ mm, $\lambda_0 = 14.6$ m; *blue circle*: dropped volume = 4.6 m^3, altitude $H = 56$ m, $\eta_{max} = 1.4$ mm, $\lambda_0 = 15.2$ m), and the white and blue squares are for the helicopter BV-107 using the 1,000-gallon Griffith helibucket (*white square*: dropped volume = 3.8 m^3, altitude $H = 12$ m, $\eta_{max} = 1.7$ mm, $\lambda_0 = 5.5$ m; *blue square*: dropped volume = 3.8 m^3, altitude $H = 16$ m, $\eta_{max} = 1.4$ mm, $\lambda_0 = 6.7$ m).

The length L_G and and the width λ_G of the coverage level $\eta_{0.5} = 0.5$ GPC ≈ 0.2 L/m^2 vary as (Legendre et al. 2013)

$$L_G = U_a T + f_1 \lambda_G, \quad \lambda_G = f_2 d_S q^{1/5}. \tag{18.}$$

The length L_G is roughly given by $U_a T$, the distance traveled by the airtanker during the drop, which needs to be corrected by a longitudinal dispersion correlated as $f_1 \lambda_G$ to the transverse dispersion of the liquid that controls the pattern width, λ_G. The relevant length scale for the evolution of the width λ_G is $d_S = \sqrt{S}$ based on the area S of the tank exit. For the standard systems using gravity, we have $f_2 \approx 27$, while for the Boeing 747 pressurized jet system, we have $f_2 \approx 58$. The evolution of $\lambda_G \approx q^{1/5}$ observed from ground tests is consistent with the transverse expansion of millimetric liquid jets in cross flow (Broumand & Birouk 2016) and the recent numerical simulations of large liquid jets in conditions corresponding to aerial firefighting (Rouaix et al. 2023). The distribution of the coverage level η along the transverse direction Y follows a Gaussian distribution (see **Figure 8***c*),

$$\eta = \eta_{max} \exp\left(-\frac{Y^2}{2\lambda_0^2}\right), \tag{19.}$$

where η_{max} is the maximum coverage and λ_0 is the standard deviation.

7.2. Rainfall Interception by Vegetation

The deposition of the dropped liquid on vegetation in the form of droplets is an extremely rich problem encompassing various topics that have been extensively investigated. The interaction between a droplet and a substrate depends on several factors: the impact conditions (droplet size and

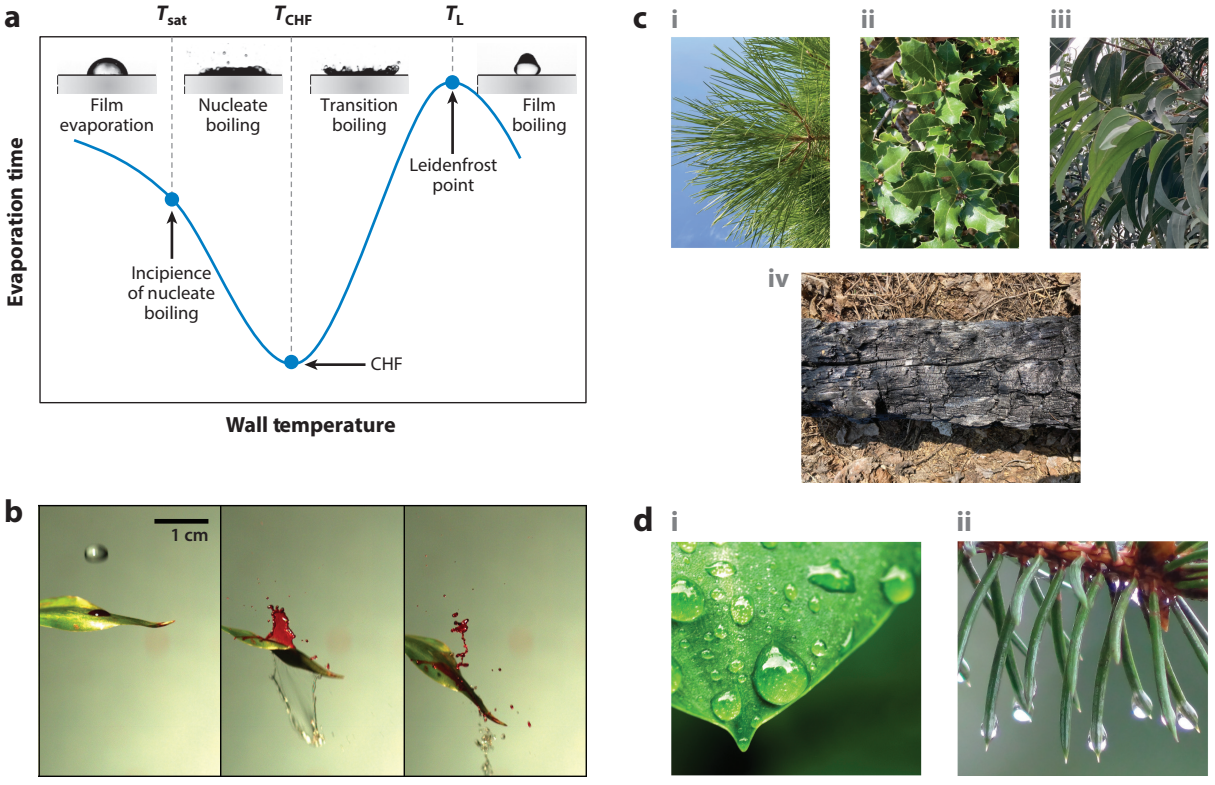

Figure 9

(*a*) Droplet evaporation regimes as a function of the substrate temperature: T_{sat} is the saturation temperature, T_{CHF} is the critical heat flux (CHF) temperature, and T_L is the Leidenfrost temperature. Panel adapted from Liang & Mudawar (2017) with permission. (*b*) Wetted leaf impacted by a droplet. Panel reprinted from Gilet & Bourouiba (2015) with permission. (*c*) Typical substrates relevant in the context of firefighting: (*i*) Aleppo pine (*Pinus halepensis*), (*ii*) kermes oak (*Quercus coccifera*), (*iii*) eucalyptus, and (*iv*) burnt wood. (*d*) Water retention by a flat leaf (*i*) and needles (*ii*).

velocity), the fluid rheology, the substrate's characteristics (inclination, elasticity, wetting properties, temperature, humidity, porosity, etc.), and the ambient conditions (temperature and wind). Many possible combinations exist, and depending on the combination of these factors, the droplet can spread, bounce, splash, run off, levitate, evaporate, and so on. This complexity is increased by the specific rheology of the retardant and the different possible substrates (types of leaves, wood, burned fuel, etc.), as shown in **Figure 9**. In the following, basic descriptions are provided of the phenomena of greatest importance for the firefighting application: droplet impact, evaporation, surface retention, and liquid interception by the canopy.

7.2.1. Impact on a substrate. The problem of droplet impact on a dry or wet substrate has been extensively investigated, and several reviews have reported the progress made in this problem that is still being intensively investigated (Yarin 2006, Josserand & Thoroddsen 2016, Wildeman et al. 2016, Villermaux 2020, Lohse 2022). During impact, the initial momentum of the droplet normal to the substrate is redirected along the substrate surface. During this process, the droplet deforms along the substrate surface with a transfer of the kinetic energy into surface energy and viscous dissipation inside the droplet. For a deformable substrate or exiting film, part of the kinetic energy is also transferred to the substrate deformation or to the film drainage. With sufficient initial

momentum, the liquid initially constitutive of the droplet can then accumulate in a toroidal rim and degenerate into radial ligaments that break into droplets. The liquid remaining in contact with the wall at the end of the droplet spreading then retracts due to the capillary force and can remain on the substrate or bounce depending on the remaining kinetic energy available at the end of the droplet contraction. Different regimes of droplet spreading can be observed depending on the condition of impact (described using, Re_d and We_d, the Reynolds and Weber numbers at impact and the angle of impact), as well as the advancing contact angle, the surface roughness, and the ambient conditions (Garcia-Geijo et al. 2020, 2021; de Goede et al. 2021). During the early stage of the spreading, the contact is characterized by the formation of a lamella and a droplet rim with base radius $r(t)$ that evolves according to $r(t) = (1.5dv_d t)^{1/2}$ (Gordillo et al. 2019), and an air bubble can be entrapped (Bouwhuis et al. 2012). For a soft impact, the combination of a high viscous fluid (such as the retardant) and a small contact angle results in a base radius $r(t)$ that follows the Tanner law $r(t) \sim t^{1/10}$, while for rapid spreading an inertial evolution of the form $r(t) \sim t^{1/2}$ is observed (Tanner 1979, Bonn et al. 2009, Winkels et al. 2012).

An energy balance is often used to describe the spreading factor $\beta = d_{max}/d$, where d_{max} is the maximum diameter of the droplet during impact. The initial kinetic energy $E_k^0 = \pi/12 d^3 \rho_L v_d^2$ and surface energy E_s^0 ($E_s^0 = \pi\sigma d^2$ if the droplet is spherical) at the moment of impact are transferred into surface energy E_s' of the flattened droplet at the moment of maximum droplet spread, substrate energy E_m', and dissipated energy E_{diss} as $E_k^0 + E_s^0 = E_s' + E_{diss} + E_m'$. Based on such an energy balance approach, different models for β have been proposed [see Yarin (2006), Attané et al. (2007), Josserand & Thoroddsen (2016), and Wildeman et al. (2016) for reviews, as well as an alternative approach based on momentum conservation by Gordillo et al. (2019) and Villermaux (2020)]. The energy transfer to the substrate E_m was proposed by Pepper et al. (2008), who considered a fixed circular membrane with a maximum displacement at the center. Reported below is the model proposed by Mao et al. (1997) for a rigid substrate ($E_m' = 0$), which is in good agreement with a large amount of literature with data ranges for impact velocities, viscosities, static contact angles, and droplet sizes relevant to the problem under consideration here:

$$\left[\frac{1}{4}(1-\cos\theta) + 0.2\frac{We_d^{0.83}}{Re_d^{0.33}}\right]\left(\frac{d_{max}}{d_0}\right)^3 - \left(\frac{We_d}{12}+1\right)\left(\frac{d_{max}}{d_0}\right) + \frac{2}{3} = 0, \qquad 20.$$

where θ is the static contact angle between the substrate and the liquid. The prefactor and exponents in the We_d/Re_d term are fitted parameters deduced from experimental measurements.

Mundo et al. (1995) proposed the criterion that droplets will splash on rigid dry surfaces if the condition $We_d^{1/2} Re_d^{1/4} > K$ is satisfied, with $K = 57.7$, while the condition for droplet splashing on preexisting liquid films of different viscosities and thicknesses e_0 takes the form $We_d\, Oh^{-2/5} > 2{,}100 + 5{,}880(e_0/d)^{1.44}$ (Cossali et al. 1997). Discussions of the effect of the surface roughness on K and a detailed description of the splashing events have been provided by Yarin (2006), Josserand & Thoroddsen (2016), and Garcia-Geijo et al. (2021). Pepper et al. (2008) reported that the splashing behavior is strongly affected by the tension in the substrate. In the context of retardant retention, the splashing is not necessarily a bad outcome, as the droplet breaks into smaller droplets that are more easily captured on nearby leaf surfaces because of a smaller impact velocity and can actually enhance the retention of the product. The number of droplets $N_s \sim Re_d^{3/8} We_d^{3/16} \sim (We_d/Oh)^{3/8}$ (Marmanis & Thoroddsen 1996) and their diameters $d_s = d/N_s^{1/3}$ produced by the splashing event are discussed by Yarin (2006) and Josserand & Thoroddsen (2016). The deposition ($E^* < 0$) or rebound ($E^* > 0$) is determined from the estimation of the energy dissipation during the droplet expansion and then retractation, providing a rebound model expressed as a function of the spreading factor β and the static contact angle θ (Mundo et al. 1995).

7.2.2. Evaporation on a substrate. The evaporation process and the lifetime of a droplet when impacting a substrate are subjects of importance for a large range of practical applications (Liang & Mudawar 2017), and the final deposition pattern of solutes in retardant droplets is due to a complex process (Lohse 2022). The substrate temperature T_S, the impact Weber number We_d, and the substrate roughness and porosity are of major importance. **Figure 9** illustrates the different regimes of evaporation and the typical evolution of the corresponding droplet lifetime when varying the substrate temperature T_S: film evaporation, nucleate boiling, transition boiling, and film boiling. When T_S is lower than the saturation temperature T_{sat}, the droplet can evaporate while maintaining a constant surface area or a constant contact angle (Picknett & Bexon 1987). When T_S begins to exceed T_{sat}, the droplet boils on the heated substrate and small vapor bubbles are produced, which grow and merge. When increasing the substrate temperature further, the droplet lifetime decreases to reach its minimum at the critical heat flux temperature, T_{CHF}. When the substrate temperature is further increased, the droplet levitates above its own vapor; this is the Leidenfrost effect (Quéré 2013). The substrate temperature at which the droplet evaporation time reaches its maximum is called the Leidenfrost temperature, T_L, which is observed to be influenced by the ambient temperature, to increase with increasing impact velocity (Tran et al. 2012), and to vary with substrate properties such as roughness and thermal diffusivity (Wakata et al. 2023). Typically, for water droplets, the order of magnitude of the static Leidenfrost temperature is $T_L \approx 160°C$, and T_L significantly increases with the impact Weber number to 400°C for $We_d = 10$ and 450°C for $We_d = 100$ (Tran et al. 2012). Because of the insulating properties of the vapor, the evaporation is then slower, the cooling effect is less efficient, and—most problematic for aerial firefighting—the droplet becomes much more mobile on the substrate, enhancing the bouncing mechanism and reducing liquid retention on very hot substrates.

7.2.3. Impact on leaves and retention. The canopy storage capacity is the amount of water or retardant held on the canopy at the end of the drop process. The canopy storage capacity has been investigated to determine the capacity of water storage after rainfall events: It depends on the rainfall intensity, the liquid viscosity, and the environmental conditions such as wind, and it significantly varies across different types of canopy (Holder 2013). A large variety of leaves have been studied to characterize their wetting properties (Klamerus-Iwan et al. 2020). Compared to a flat substrate, the impact on leaves is more complex due to the biomechanical response of the leaf and its orientation, which can vary after successive impacts (Ginebra-Solanellas et al. 2020). Liquid retention models have been developed based on impact on flat substrate results (Dorr et al. 2018). Specific models based on the critical speed below which leaf capture occurs and above which the droplet rebounds have integrated the wavelength of the leaf grooves as the characteristic surface roughness (Cox et al. 2000).

Among the huge variety of leaves that have been considered, pine needles have been observed to be especially resistant to raindrop impacts. Lebanoff & Dickerson (2009) reviewed droplet impact on fibers and reported the results of experiments involving the specific profile of pine needles to study droplet impact, division, and spreading. They showed that the mass retention m_c as a portion of the droplet mass m_d is $m_c/m_d \sim d_f/d\, We_d^{-1/4}$, where d_f is the fiber radius. The focus on successive impacts is required to address retention efficiency. Gilet & Bourouiba (2015) identified two dominant fluid fragmentation scenarios during the impact of a leaf already wetted by a sessile droplet (**Figure 9**). The liquid can be ejected by the direct interaction between the two droplets, or the ejection can be induced by the biomechanical response of the leaf, which can be described using a damped harmonic oscillator.

Depending on the droplet size, impacts have different effects on the retention stability. The impact of large droplets results in a large change in the substrate equilibrium and enhances the splashing and projection of the liquid into smaller droplets. When small droplets impact

the surface, they progressively contribute to form larger droplets whose stability depends on the substrate inclination and the wetting properties. The droplets grow to a critical size, above which they begin to slide down the surface and drip off. This process, usually referred to as runoff, is governed by the movement of the liquid droplets on the substrate (Furmidge 1962b). The runoff criteria for a single droplet on a substrate of inclination α can be determined by considering the force balance acting on the droplet. The volume V_c of the largest droplet that can stick on the surface is given by the balance between the weight of the droplet and the interfacial force acting along the contact line cl as

$$\rho_L g V_c \sin(\alpha_c) = K\,(\cos(\theta_R) - \cos(\theta_A)), \qquad 21.$$

where $K = \int_{cl} \cos(\theta_{cl})\,\sin(\beta_{cl})\,d\ell/(\cos(\theta_R) - \cos(\theta_A))$ is a characteristic length depending on the wetting conditions and the contact line shape, θ_{cl} is the local contact angle, and β_{cl} is the angle between the direction perpendicular to the sliding direction and the unit normal to the contact line pointing out from the droplet. This relation gives the runoff criteria for the droplet size at a given angle, or the required angle for a given droplet size. By considering $K \approx w$, w being the width of the droplet, one can arrive at the original results proposed by Furmidge (1962b). The expression for K proposed by Dussan (1985) is well approximated by $K \approx 2^{1/3} d$, a value close to the droplet width w, and is in good agreement with experiments and numerical simulations conducted for a large range of hystereses [up to $\theta_A - \theta_R = 100°$ in Maglio & Legendre (2014)].

When the substrate is inclined with an angle $\alpha \geq \alpha_c$, the droplet sliding at velocity v_S induces a viscous resistance due to the friction with the substrate, $\sim \mu_L d v_S$, and the amended force balance is $\rho_L g V_c \sin(\alpha) - K(\cos(\theta_R) - \cos(\theta_A)) \sim \mu_L d v_S$. Combined with the runoff criteria (Equation 21), the sliding velocity is expressed using the capillary number $Ca = \mu_L v_s/\sigma$ and the bond number $Bo = \rho_L g d^2/\sigma$ as

$$Ca \sim Bo\,[\sin(\alpha) - \sin(\alpha_c)]\,, \qquad 22.$$

in agreement with experiments (Le Grand et al. 2005) and numerical simulations (Maglio & Legendre 2014) for Newtonian fluids of various viscosities (up to 100 times the viscosity of water). Given a uniform and homogeneous spray of small droplets over leaves of various plants in the context of agricultural sprays, the volume of spray retained per unit surface scales as $\sim \theta_M[\sigma(\cos(\theta_R) - \cos(\theta_A))/\rho_L]^{1/2}$, where θ_M is the arithmetic mean of θ_A and θ_R (Furmidge 1962a), which shows that the values of the advancing and receding contact angles are important factors governing spray retention. Furmidge (1962a) also reported that the variation in retention is closely associated with the irregularities of the leaf surface. Among the tested leaves, the highest retention is found on the lower surface of blackcurrant leaves, whose surface contours show a series of sharp peaks corresponding to a very prominent vein structure. The leaves with the smoothest surfaces have the lowest retention. In the context of agrochemical applications, wetting properties of some leaves are reported by Taylor (2011).

The penetration of a dropped liquid in a canopy is an important issue that should be addressed with 3D modeling (Tomé 2004). The arrangement of different types of vegetation such as trees, shrubs, herbs, and dead fuel in the soil have to be integrated to provide a realistic model, which can be achieved using fractal methods or a virtual representation of the vegetation, as illustrated in **Figure 10**. Such vegetation models can serve as the basis for computational fluid dynamics simulations that use methods, such as volume of fluid or level set methods, to simulate the evolution of the droplet cloud in the air and its interaction with the vegetation (Calogine et al. 2007).

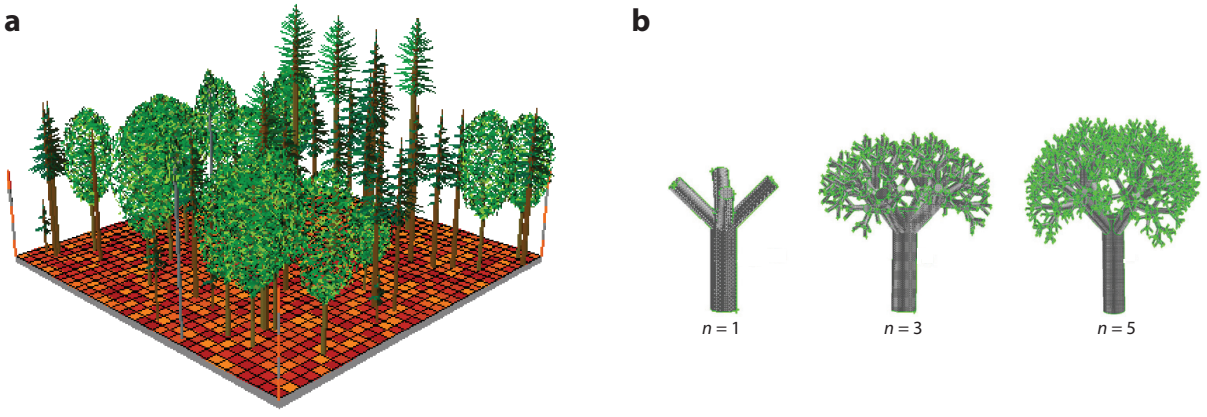

Figure 10

Three-dimensional representations of vegetation using (*a*) a virtual reality model created with the Stand Visualization System developed at the US Forest Service by R.J. McGaughey and (*b*) an iterated function system, whereby an initial set is transformed by n contracting transformations and then glued together. Panels adapted with permission from (*a*) Tomé (2004) and (*b*) Calogine et al. (2007).

8. CONCLUSION

This review gives an overview of the fluid dynamics of airtanker firefighting, a fascinating application involving rich and varied physical phenomena. During airtanker spraying, the shape of the liquid column that develops under the aircraft (linear versus parabolic) indicates whether the ejected liquid is under the acceleration of gravity or is stabilized to a fixed velocity at the tank exit. The spectacular liquid meteors that detach from the front of the liquid column suggest the development of a multimodal Rayleigh–Taylor instability. These liquid meteors travel at a high velocity, which reflects the velocity of the aircraft at ejection, and may impact the ground at high velocity if not fully atomized beforehand, resulting in a drop pattern with areas of high concentration. A droplet cloud produced by the atomization of the liquid column comprises a multimodal distribution of droplet sizes, ranging from 10 μm to 1 cm, that are produced by a very intense and efficient surface shear breakup mechanism, in which ligaments and bags are suspected to play a major role. The lifetime of the cloud is very short compared to that of an atmospheric cloud, but droplets smaller than 100 μm, if not captured before by the aircraft wake, have enough time to be dispersed by the wind or evaporate. After a travel time ranging from a few seconds to tens of minutes, depending on their size, the droplets finally reach the ground, where they impact on the vegetation, bounce, spread, levitate, splash, run off, evaporate, and so on. The liquid's interception by the canopy, with its important diversity of receiving substrates (from leaves to burnt wood), raises many open questions of great interest for the characterization of liquid retention efficiency. The major challenge to address in future investigations is the role of the complex rheology of retardant on all the physical mechanisms described in the review. The retardant has been optimized for firefighting operations through increasing the liquid atomization efficiency and by achieving an optimal droplet size—droplets need to be big enough to minimize wind dispersion and evaporation effects and have satisfactory penetration through the canopy, but be small enough to ensure efficient retention by the vegetation.

Among the important open questions on this topic, those that take priority involve investigations to both provide deeper understanding of the physical mechanisms involved and develop useful information for improving airtanker efficiency. These issues are listed below.

FUTURE ISSUES

1. Large-scale instabilities manifest differently depending on the airtanker. There is no convincing explanation of the origin of the large-scale instability that develops and generates meteors that detach from the liquid column front. Understanding the appearance and amplification of liquid meteors is of great importance for the development of a control strategy for a more uniform deposition of liquid on the ground.
2. What are the effective mechanisms behind the surface atomization process: ligament or bag breakup? Recent observations of ocean spraying seem to indicate the prevalence of the bag mechanism. What is the resulting size distribution, frequency, and surface density? This information is necessary for the development of an airtanker spray generation function, following research efforts deployed in the development of a sea spray generation function (Veron 2015).
3. Once formed, the droplets evolve into a very dynamic cloud that penetrates a presumably hot and windy ambient air. The droplets range over at least three orders of magnitude in size, some evolving as tracers, and others having a ballistic trajectory before impacting the ground. In such conditions a specific equation for the evolution of the droplet size distribution function could be developed using approaches similar to those used for atmospheric clouds (Shaw 2003).
4. Another issue of crucial importance relates to the complex rheology of the product used for aerial firefighting. The viscoelastic and shear-thinning properties of the product, associated with a high viscosity, engender a long list of potential investigations involving most of the problems described in this review: atomization, breakup, impact, spreading, wetting, evaporation, and splashing.

DISCLOSURE STATEMENT

The author is not aware of any biases that might be perceived as affecting the objectivity of this review.

ACKNOWLEDGMENTS

It is my pleasure to thank all colleagues and PhD and undergraduate students for all their work, interest, discussion, and contributions to our understanding of this fascinating subject. I wish to thank Alain Fontaine for introducing me to the subject by asking me to provide a simple model of the process of a liquid dropped from an aircraft—"*Cela doit être très facile!*"—and David Joubert for our collaboration in the development of the new delivery system KIOS. The US Forest Service provided the video for the supplemental material. I thank José Gordillo, Rui Ni, Chao Sun, and Roberto Zenit for comments on the manuscript. Over the last several years, my investment for this subject has been supported by the Institut de Mécanique des Fluides de Toulouse and warmly encouraged by its director, Eric Climent. Finally, I thank the Co-Editors of the *Annual Review of Fluid Mechanics* for inviting me to submit this review.

LITERATURE CITED

Abarzhi SI. 2008. Review of nonlinear dynamics of the unstable fluid interface: conservation laws and group theory. *Phys. Scr.* 2008(T132):014012

Alon U, Hecht J, Offer D, Shvarts D. 1995. Power-laws and similarity of Rayleigh-Taylor and Richtmyer-Meshkov mixing fronts at all density ratios. *Phys. Rev. Lett.* 74:534

Amorim JH. 2011a. Numerical modelling of the aerial drop of firefighting agents by fixed-wing aircraft. Part I: model development. *Int. J. Wildland Fire* 20:384–93

Amorim JH. 2011b. Numerical modelling of the aerial drop of firefighting agents by fixed-wing aircraft. Part II: model validation. *Int. J. Wildland Fire* 20:394–406

Anderson WH, Brown RE, Blatz PJ, Louie NA, Burchfield J. 1974. *Investigation of rheological properties of aerial-delivered fire retardant*. Tech. Rep. 8990-04, North. Forest Fire Lab., U.S. Forest Serv., Washington, DC

Attané P, Girard F, Morin V. 2007. An energy balance approach of the dynamics of drop impact on a solid surface. *Phys. Fluids* 19:012101

Behzad M, Ashgriz N, Mashayek A. 2015. Azimuthal shear instability of a liquid jet injected into a gaseous cross-flow. *J. Fluid Mech.* 767:146–72

Bellman R, Pennington RH. 1954. Effects of surface tension and viscosity on Taylor instability. *Q. Appl. Math.* 12:151–62

Biance AL, Clanet C, Quéré D. 2003. Leidenfrost drops. *Phys. Fluids* 15:1632–37

Bonn D, Eggers J, Indekeu J, Meunier J, Rolley E. 2009. Wetting and spreading. *Rev. Mod. Phys.* 81:739–805

Boulesteix S. 2010. *Cisaillement d'une interface gaz-liquide en conduite et entraînement de gouttelettes*. PhD Thesis, Inst. Natl. Polytech. Toulouse, France

Bouwhuis W, van der Veen RCA, Tran T, Keij DL, Winkels KG. 2012. Maximal air bubble entrainment at liquid-drop impact. *Phys. Rev. Lett.* 109(26):264501

Broumand M, Birouk M. 2016. Liquid jet in a subsonic gaseous crossflow: recent progress and remaining challenges. *Prog. Energy Combust. Sci.* 57:1–29

Calbrix C, Stoukov A, Cadière A, Roig B, Legendre D. 2023. Numerical simulation of aerial liquid drops of Canadair CL-415 and Dash-8 airtankers. *Int. J. Wildland Fire* 32(11):1515–28

Calogine D, Rimbert N, Séro-Guillaume O. 2007. Modelling of the deposition of retardant in a tree crown during fire fighting. *Environ. Model. Softw.* 22:1654–66

Chen J, Zhou Y, Antonia R, Zhou T. 2018. Characteristics of the turbulent energy dissipation rate in a cylinder wake. *J. Fluid Mech.* 835:271–300

Chou WH, Faeth GM. 1998. Temporal properties of secondary drop breakup in the bag breakup regime. *Int. J. Multiph. Flow* 24:889–912

Clift R, Gauvin WH. 1970. The motion of particles in turbulent gas streams. In *Proceedings of Chemeca Conference '70*, Vol. 1, pp. 14–28. London: Butterworth

Cossali GE, Coghe A, Marengo MT. 1997. Characteristics of the turbulent energy dissipation rate in a cylinder wake. *Exp. Fluids* 22:463–72

Cox SJ, Salt DW, Lee BE, Ford MG. 2000. A model for the capture of aerially sprayed pesticide by barley. *J. Wind Eng. Ind. Aerodyn.* 87:217–30

Davies RM, Taylor GI. 1950. The mechanics of large bubbles rising through extended liquids and through liquids in tubes. *Proc. R. Soc. A* 200:375–90

de Goede T, de Bruin K, Shahidzadeh N, Bonn D. 2021. Droplet splashing on rough surfaces. *Phys. Rev. Fluids* 6:043604

Deike L. 2022. Mass transfer at the ocean–atmosphere interface: the role of wave breaking, droplets, and bubbles. *Annu. Rev. Fluid Mech.* 54:191–224

Dhar P, Mishra SR, Gairola A, Samanta D. 2020. Delayed Leidenfrost phenomenon during impact of elastic fluid droplets. *Proc. R. Soc. A* 476:20200556

Dorr GJ, Kempthorne DM, Mayo LC, Forster WA, Zabkiewicz JA, et al. 2014. Towards a model of spray–canopy interactions: interception, shatter, bounce and retention of droplets on horizontal leaves. *J. Fluid Mech.* 290:94–101

Dussan EB. 1985. On the ability of drops or bubbles to stick to non-horizontal surfaces of solids. Part 2. Small drops or bubbles having contact angles of arbitrary size. *J. Fluid Mech.* 151:1–20

Furmidge CGL. 1962a. Physico-chemical studies on agricultural sprays. IV. The retention of spray liquids on leaf surfaces. *J. Sci. Food Agric.* 13:127–40

Furmidge CGL. 1962b. Studies at phase interfaces. I. The sliding of liquid drops on solid surfaces and a theory for spray retention. *J. Colloid Sci.* 17:309–24

Garcia-Geijo P, Quintero E, Riboux G, Gordillo J. 2021. Spreading and splashing of drops impacting rough substrates. *J. Fluid Mech.* 917:A50
Garcia-Geijo P, Riboux G, Gordillo J. 2020. Inclined impact of drops. *J. Fluid Mech.* 897:A12
Gatignol CGL. 1983. The Faxen formulae for a rigid particle in an unsteady non-uniform Stokes flow. *J. Mécan. Théor. Appl.* 1:143–60
George CW, Johnson GM. 1990. *Developing air tanker performance guidelines*. Tech. Rep. INT-GTR-268, US Forest Serv. Intermt. Res. Stn., Ogden, UT
Gilet T, Bourouiba L. 2015. Fluid fragmentation shapes rain-induced foliar disease transmission. *J. R. Soc. Interface* 12:20141092
Ginebra-Solanellas RM, Holder CD, Lauderbaugh LK, Webb R. 2020. The influence of changes in leaf inclination angle and leaf traits during the rainfall interception process. *Agric. Forest Meteorol.* 285–86:107924
Gordillo JM, Riboux G, Quintero ES. 2019. A theory on the spreading of impacting droplets. *J. Fluid Mech.* 866:298–315
Hinze JO. 1955. Fundamentals of the hydrodynamic mechanism of splitting in dispersion processes. *AIChE J.* 1(3):289–95
Holder CD. 2013. Effects of leaf hydrophobicity and water droplet retention on canopy storage capacity. *Ecohydrology* 6:483–90
Ito T, Kato H, Goda Y, Tagawa S, Negishi E. 2010. *Water-dropping aerodynamics for fire-fighting amphibian.* Paper presented at the 27th International Council of the Aeronautical Sciences, Nice, France, Sept. 19
Josserand C, Thoroddsen ST. 2009. Drop impact on a solid surface. *Annu. Rev. Fluid Mech.* 8:365–91
Kataoka I, Ishii M, Mishima K. 1983. Generation and size distribution of droplet in annular two-phase flow. *Trans. ASME J. Fluids Eng.* 105:230–38
Keshavarz B, Houze EC, Koerner MR, Moore JR, Cotts PM, et al. 2015. Studying the effects of elongational properties on atomization of weakly viscoelastic solutions using Rayleigh Ohnesorge Jetting Extensional Rheometry (ROJER). *J. Non-Newton. Fluid Mech.* 222:171–89
Keshavarz B, Houze EC, Moore JR, Koerner MR, McKinley MC. 2016. Ligament mediated fragmentation of viscoelastic liquids. *Phys. Rev. Lett.* 117:154502
Klamerus-Iwan A, Łagan S, Zarek M, Słowik-Opoka E, Wojtan B. 2020. Variability of leaf wetting and water storage capacity of branches of 12 deciduous tree species. *Forests* 11:1158
Koga JO. 1981. Direct production of droplets from breaking wind-waves: its observation by a multi-colored overlapping exposure photographing technique. *Tellus* 33:552–63
Lake A, Marchant A. 1983. The use of dimensional analysis in a study of drop retention on barley. *Pestic. Sci.* 14:638–44
Lebanoff A, Dickerson A. 2020. Drop impact onto pine needle fibers with non-circular cross section. *Phys. Fluids* 32:092113
Lee J, Laan N, De Bruin K, Skantzaris G, Shahidzadeh H, et al. 2016. Universal rescaling of drop impact on smooth and rough surfaces. *J. Fluid Mech.* 786:R4
Legendre D, Becker B, Alméras E, Chassagne A. 2013. Air tanker drop patterns. *Int. J. Wildland Fire* 23(2):272–80
Le Grand N, Daerr A, Limat L. 2005. Shape and motion of drops sliding down an inclined plate. *J. Fluid Mech.* 541:293–315
Lewis DJ. 2022. The instability of liquid surfaces when accelerated in a direction perpendicular to their plane. *Proc. R. Soc. A* 202:81–96
Lhuissier H, Villermaux E. 2009. Bursting bubbles. *Phys. Fluids* 21:091111
Lhuissier H, Villermaux E. 2012. Bursting bubble aerosols. *J. Fluid Mech.* 696:5–39
Liang G, Mudawar I. 2017. Review of drop impact on heated walls. *Int. J. Heat Mass Transf.* 106:103–26
Lohse D. 2022. Fundamental fluid dynamics challenges in inkjet printing. *Annu. Rev. Fluid Mech.* 54:349–82
Lubarsky E, Shcherbik D, Bibik A, Gopala Y, Zinn B. 2012. Fuel jet in cross flow—experimental study of spray characteristics. *Adv. Fluid Dyn.* 4:59–80
Maglio M, Legendre D. 2014. Numerical simulation of sliding drops on an inclined solid surface. In *Computational and Experimental Fluid Mechanics with Applications to Physics, Engineering and the Environment*, pp. 47–69. Cham, Switz.: Springer Int.

Makhnenko I, Alonzi ER, Fredericks SA, Colby CM, Dutcher CS. 2021. A review of liquid sheet breakup: perspectives from agricultural sprays. *J. Aerosol Sci.* 157:105805

Mao T, Kuhn DCS, Tran H. 1997. Spread and rebound of liquid droplets upon impact on flat surfaces. *AIChE J.* 43:2169–79

Marmanis H, Thoroddsen E. 1996. Scaling of the fingering pattern of an impacting drop. *Phys. Fluids* 8:1344–46

Marmottant P, Villermaux E. 2009. On spray formation. *J. Fluid Mech.* 498:73–38

Mashayek A, Ashgriz N. 2011. Atomization of a liquid jet in a crossflow. In *Handbook of Atomization and Sprays*, ed. N Ashgriz, pp. 657–83. New York: Springer

Maxey MR, Riley JJ. 1983. Equation of motion for a small rigid sphere in a nonuniform flow. *Phys. Fluids* 26:883–89

Mueller JA, Veron F. 2009. A sea state dependent spume generation function. *J. Phys. Oceanogr.* 39:2363–72

Mundo C, Sommerfeld M, Tropea C. 1995. Characteristics of the turbulent energy dissipation rate in a cylinder wake. *Int. J. Multiph. Flow* 21:151–73

No SY. 2015. A review on empirical correlations for jet/spray trajectory of liquid jet in uniform cross flow. *J. Spray Combust. Dyn.* 7:283–314

Pappa AA, Tzamtzis NE, Statheropoulos MK, Liodakis SE, Parissakis GK. 1995. A comparative study of the effects of fire retardants on the pyrolysis of cellulose and *Pinus halepensis* pine-needles. *J. Anal. Appl. Pyrolys.* 31:85–100

Pepper RE, Courbin L, Stone HA. 2008. Splashing on elastic membranes: The importance of early-time dynamics *Phys. Fluids* 20:082103

Pilch M, Erdman C. 1987. Use of breakup time data and velocity history data to predict the maximum size of stable fragments for acceleration-induced breakup of a liquid drop. *Int. J. Multiph. Flow* 13(6):741–57

Picknett RG, Bexon R. 1977. The evaporation of sessile or pendant drops in still air. *J. Colloid Interface Sci.* 61(2):336–50

Quéré D. 2013. Leidenfrost dynamics. *Annu. Rev. Fluid Mech.* 45:19–215

Qureshi S, Altman A. 2018. *Studying fluid breakup and dispersion to predict aerial firefighting ground drop patterns*. Paper presented at the 2018 AIAA Aerospace Sciences Meeting, Kissimee, FL, Jan. 8

Rayleigh L. 1883. Investigations of the character of the equilibrium of an incompressible heavy fluid of variable density. *Proc. Lond. Math. Soc.* s1-14:170–77

Rouaix C, Stoukov A, Bury Y, Joubert D, Legendre D. 2023. Liquid jet breakup in gaseous crossflow injected through a large diameter nozzle. *Int. J. Multiph. Flow* 163:104419

Renksizbulut M, Yuen MC. 1983. Experimental study of droplet evaporation with variable properties and internal circulation at intermediate Reynolds numbers. *Int. J. Multiph. Flow* 14:189–202

Rimbert N. 2003. *Contribution à l'étude de la pulvérisation et de la dispersion dans l'air de fluides newtoniens et non-newtoniens. Application au largage aérien d'eau et de mélanges retardants*. PhD Thesis, Inst. Natl. Polytech. Lorraine, Nancy, France

Rimbert N, Castanet G. 2011. Crossover between Rayleigh-Taylor instability and turbulent cascading atomization mechanism in the bag-breakup regime. *Phys. Rev. E* 84:016318

Rui N. 2024. Deformation and breakup of bubbles and drops in turbulence. *Annu. Rev. Fluid Mech.* 56:319–47

Satoh K, Kuwahara K, Yang KT. 2000. Experimental and numerical simulations of flow patterns of dropping water from fire-fighting helicopters. In *Proceedings of the ASME 2000 International Mechanical Engineering Congress and Exposition*, Vol. 5: *Heat Transfer*, pp. 57–64. Orlando, FL: ASME

Shaw RA. 2003. Particle-turbulence interactions in atmospheric clouds. *Annu. Rev. Fluid Mech.* 35:183–227

Snoeijer JH, Brunet P, Eggers J. 2009. Maximum size of drops levitated by an air cushion. *Phys. Rev. E* 79:036307

Steiner M, Smith JA, Uijlenhoet R. 2004. A microphysical interpretation of the radar reflectivity-rain rate relationship. *J. Atmos. Sci.* 61:1114–31

Suter A. 2000. *Drop testing airtankers: a discussion of the cup-and-grid method*. Tech. Rep. 0057-2868-MTDC, Technol. Dev. Cent., US Forest Serv., Missoula, MT

Tanner LH. 1979. The spreading of silicone oil drops on horizontal surfaces. *J. Phys. D* 12:1473

Taylor P. 2011. The wetting of leaf surfaces. *Curr. Opin. Colloid Interface Sci.* 16:326–34

Testik FY, Barros AP. 2007. Towards elucidating the microstructure of warm rainfall: a survey. *Rev. Geophys.* 45:RG2003

Tomé MJC. 2004. *Modelação da nuvem de retardante químico: optimização no combate aos fogos florestais*. PhD Thesis, Univ. Aveiro, Port.

Tran T, Staat HJJ, Prosperetti A, Sun C, Lohse D. 2012. Drop impact on superheated surfaces. *Phys. Rev. Lett.* 108:036101

Troitskaya Y, Kandaurov A, Ermakova O, Kozlov D, Sergeev D, Zilitinkevich S. 2018. The "bag breakup" spume droplet generation mechanism at high winds. Part I: spray generation function. *Geophys. Res. Lett.* 48:2167–88

Vallon R, Abid A, Anselmet F. 2021. Multimodal distributions of agricultural-like sprays: a statistical analysis of drop population from a pressure-atomized spray. *Phys. Rev. Fluids* 6(2):023604

Veron F. 2015. Ocean spray. *Annu. Rev. Fluid Mech.* 47:507–31

Veron F, Hopkins C, Harrison EL, Mueller JA. 2012. Sea spray spume droplet production in high wind speeds. *J. Phys. Oceanogr.* 39:L16602

Villermaux E. 2007. Fragmentation. *Annu. Rev. Fluid Mech.* 39:419–27

Villermaux E. 2020. Fragmentation. *J. Fluid Mech.* 898:P1

Villermaux E, Bossa B. 2009. Single drop fragmentation determines size distribution of raindrops. *Nat. Phys.* 5:697–702

Villermaux E, Bossa B. 2010. Size distribution of raindrops. *Nat. Phys.* 6:232

Wakata Y, Zhu N, Chen X, Lyu S, Lohse D, et al. 2023. How roughness and thermal properties of a solid substrate determine the Leidenfrost temperature: experiments and a model. *Phys. Rev. Fluids* 8:L061601

Wildeman S, Visser CW, Sun C, Lohse D. 2016. On the spreading of impacting drops. *J. Fluid Mech.* 805:636–55

Wilson JE, Grib SW, Ahmad AD, Renfro MW, Adams SA, Salaimeh AA. 2018. Study of near-cup droplet breakup of an automotive electrostatic rotary bell (ESRB) atomizer using high-speed shadowgraph imaging. *Coatings* 8(5):174

Winkels K, Weijs J, Eddi A, Snoeijer JAS. 2012. Initial spreading of low-viscosity drops on partially wetting surfaces. *Phys. Rev. E* 85:055301

Wu PK, Kirkendall KA, Fuller RP, Nejad AS. 1997. Breakup processes of liquid jets in subsonic crossflows. *J. Propul. Power* 13(1):64–73

Yarin AL. 2006. Drop impact dynamics: splashing, spreading, receding, bouncing, . . . *Annu. Rev. Fluid Mech.* 38:159–92

Zhao X, Zhou P, Yan X, Weng Y, Yang XL. 2018. *Numerical simulation of the aerial drop of water for fixed-wing airtankers.* Paper presented at the 31st Congress of the International Council of the Aeronautical Sciences, Belo Horizonte, Brazil, Sept. 9